University of Reading

School of Mathematics, Meteorology and Physics

Numerical Modelling of Tidal Bores using a Moving Mesh

G.M.Morrison

This dissertation is submitted to the Department of Mathematics and Meteorology in partial fulfilment of the requirements for the degree of Master of Science

August 2008

Acknowledgements

Declaration

I confirm that this is my own work and the use of all material from other sources has been properly and fully acknowledged.

Abstract

This dissertation considers different approaches to numerically modelling tidal bores, which are features involving steep gradients and discontinuities. We first give a brief background on how and where tidal bores form and then go on to derive the shallow water equations which can be applied in this situation as the length scale of our problem is much larger than the depth of water.

We then have a review of three different finite element methods which were investigated by White et al. (2006), with particular attention to how well they perform when applied to discontinuities. In chapter three we go on to investigate different approaches to adapting the mesh used in the numerical model, before focusing on two methods which move the nodes with time.

In chapters four and five we go on to apply these methods in two different models. A simple model with a rectangular domain is investigated in chapter four, using various initial conditions. The second model is based on the tidal flow in the Daly River, Australia and the two moving mesh methods are applied to this in chapter five.

Contents

List of Figures

Chapter 1

Tidal Bores

In a river estuary there is often a conflict of flow due to the tidal flows of the sea meeting the river effluence. This can result in a phenomenon known as a tidal bore occurring either in the estuary and/or further upstream, as the incoming tide forces water up the river against the current. A tidal bore is simply a steep fronted wave or series of waves which travel upstream along the river. It can take one of two forms: a breaking bore or an undular bore. A breaking bore is rare and only usually occurs for a short period of time, for instance as the bore travels over a particularly shallow stretch of the river.

Figure 1.1: Tidal bore on the River Severn, England. (Picture sourced from [26], map [27].)

Tidal bores do not occur in all rivers. They are most likely to occur in estuaries which have a large tidal range and which narrow and/or shallow rapidly. It is thought there are about 100 rivers worldwide which experience tidal bores. The largest one in Britain occurs on the River Severn which reaches heights of 3m and speeds of 15kmh^{-1} [26]. In the Zheijang Province in China a large bore forms on the Qiantang River known as the 'Silver' or 'Black Dragon'. The river flows into Hangzhou Bay which is around 100km wide. Within the bay is a peninsula of reclaimed land which narrows the estuary down to several kilometers suddenly. The river bed also rises rapidly

Figure 1.2: Tidal bore on the Qiatang River, China. (Picture sourced from [26], map [27].)

and so as the tide comes in water is forced into a rapidly decreasing channel causing a bore to form which has been thought to have reached 8.9m high and travels at speeds of around 30kmh^{-1} [26]. The bore which has been

Figure 1.3: Tidal bore on the Rio Araguari, Brazil. (Picture sourced from [26], map [27].)

classed as the most dangerous in the world forms on the Rio Araguari in Amapa State, Brazil. This river drains into the Atlantic Ocean close to the Amazon. It has been sighted breaking as far out to sea as 10km due to the river basin extending so far out and 150km inland. It has an average height of 2-4m and travels around 25kmh^{-1} [26].

Very little is known about the effects tidal bores have on the river environment which is why producing accurate numerical models would be beneficial alongside field studies. The bore has an effect on the sediment transport taking place within a river which then affects other organisms. For instance, in the Amazon, piranhas feed off matter which is suspended after the bore has passed and in the Bay of Fundy the eggs released by striped bass are carried up the river by the bore [7]. There are also effects on the river banks

2

due to the increased turbulence and large velocities of the water. This can lead to erosion and damage to vegetation and ecosystems along river banks. This is the main reason tidal bores are studied.

A tidal bore is also known as a hydraulic jump. When a liquid is flowing in a channel of fixed width at a high velocity, say u_2, and meets a liquid with a lower velocity, u_1, the elevation increases. This allows the fluid which had been travelling at velocity u_2 to convert some of its kinetic energy to potential energy. Hydraulic jumps can be stationary, for example after a weir, or moving, as in the case of a tidal bore. Hydraulic jumps only occur in
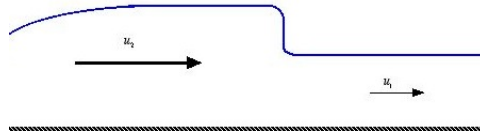
Figure 1.4: The change in elevation occuring where a fast flowing fluid encounters a slower moving fluid.

supercritical flows. These are where the flow velocity, which can be thought of as the speed at which a leaf being carried along by the river would travel, is greater than the wave velocity, the speed of ripples caused by an object falling into the river. If the flow velocity is less than the wave velocity the flow is said to be subcritical. The wave velocity in shallow water is $c = \sqrt{gH}$ where g is the gravitaional constant and H is the depth of the fluid. The Froude number is defined as the ratio of the flow and wave velocities and is given by

$$Fr = \frac{u}{\sqrt{gH}} \tag{1.1}$$

where u is the flow velocity of the fluid, H is the depth of the fluid and g is the gravitational constant. Therefore for a hydraulic jump, or tidal bore, to occur the Froude number must be greater than 1.

1.1 Basic Equations

1.1.1 Momentum Equation

According to Newton's second law of motion, the rate of change of motion of a body is equal to the sum of forces acting on the body. Assuming that the fluid is non-viscous and incompressible the only forces acting on a material element are the pressure force and the gravitational force. Therefore in three dimensions taking x, y to be the horizontal plane and z to be vertically upwards

$$\frac{D\mathbf{v}}{Dt} = -\frac{1}{\rho}\nabla\mathbf{p} - \mathbf{g} \tag{1.2}$$

where $\mathbf{v} = (u, v, w)$ is the velocity, ρ is the density and p the pressure of the fluid and $\mathbf{g} = (0, 0, -g)$ is the gravitational acceleration. Note that we are using the material derivative which measures the change of a variable in

time following a particular fluid particle,

$$\frac{D}{Dt} = \frac{\partial}{\partial t} + u\frac{\partial}{\partial x} + v\frac{\partial}{\partial y} + w\frac{\partial}{\partial z}. \tag{1.3}$$

This is the momentum equation in a non-inertial frame. However, as the Earth is constantly in motion in space it is more correct to obtain this equation with respect to variables measured relative to the earth, i.e. relative to a *rotating reference frame*.

In the following the subscript f will denote a variable in the fixed reference frame and the subscript r will denote a variable in the rotating reference frame. Consider a material element at position $\mathbf{x}_r$. Its velocity $\mathbf{v}_r = D\mathbf{x}_r/Dt$ relative to an inertial frame is given by

$$\mathbf{v}_f = \mathbf{v}_r + \mathbf{\Omega} \times \mathbf{x}_r \tag{1.4}$$

where $\mathbf{\Omega}$ is the angular velocity vector. On Earth, as any other sphere, the angular velocity vector at any latitude ϕ is given by $\mathbf{\Omega} = \Omega(0, \cos\phi, \sin\phi)$ with Ω being the rotation rate of the earth. Similarly, the acceleration relative to an inertial reference frame is

$$\left(\frac{D\mathbf{v}_f}{Dt}\right)_f = \frac{D\mathbf{v}_f}{Dt} + (\mathbf{\Omega} \times \mathbf{v}_f) \tag{1.5}$$

Substituting in the velocity from equation (1.4), we obtain

$$\left(\frac{D\mathbf{v}_f}{Dt}\right)_f = \frac{D}{Dt}(\mathbf{v}_r + \mathbf{\Omega} \times \mathbf{x}_r) + \mathbf{\Omega} \times (\mathbf{v}_r + \mathbf{\Omega} \times \mathbf{x}_r)$$

$$= \frac{D\mathbf{v}_r}{Dt} + 2\mathbf{\Omega} \times \mathbf{v}_r + \mathbf{\Omega} \times (\mathbf{\Omega} \times \mathbf{x}_r) \tag{1.6}$$

for the acceleration apparent in an inertial frame.

As can be seen there are two "corrections" which are made to take account of the rotating reference frame. The first, $2\mathbf{\Omega} \times \mathbf{v}_r$, is known as the *Coriolis acceleration* which is perpendicular to both the motion of the parcel of air and the planetary vorticity, $\mathbf{\Omega}$. The second term, $\mathbf{\Omega} \times (\mathbf{\Omega} \times \mathbf{x}_r)$, is the *centrifugal acceleration* of the air parcel due to the earth's rotation. This acts perpendicular to and away from the axis of rotation and is often absorbed into the gravitational acceleration, which will be assumed here.

Therefore our momentum equation (1.2) in a rotating reference frame is

$$\frac{D\mathbf{v}}{Dt} + 2\mathbf{\Omega} \times \mathbf{v} = -\frac{1}{\rho}\nabla p - \mathbf{g}. \tag{1.7}$$

1.1.2 The Continuity Equation

This equation is based on the concept of the conservation of mass. Consider a fixed, infinitely small, element of volume in a fluid (as shown in figure 1.5) which has density ρ and velocity $\mathbf{v} = (u, v, w)$ at the centre. Mass flows constantly through the sides, for instance, the left hand side of the element will have a mass flux of

$$\left\{\rho u - \frac{1}{2}\frac{\partial}{\partial x}(\rho u)\delta x\right\}\delta y \delta z$$

4
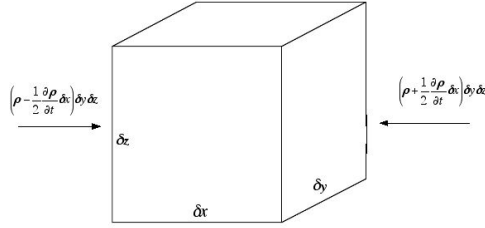
Figure 1.5: The flow of mass through a fixed element of fluid.

and similarly the right hand side will have

$$\left\{ \rho u + \frac{1}{2}\frac{\partial}{\partial x}(\rho u)\delta x \right\} \delta y \delta z$$

Therefore, taking all sides into account the net flow of mass into the volume element will be

$$-\left\{ \frac{\partial}{\partial x}(\rho u) + \frac{\partial}{\partial y}(\rho v) + \frac{\partial}{\partial z}(\rho w) \right\} \delta x \delta y \delta z$$

and taking the limit of this as the volume goes to zero the rate of increase of mass per unit volume is

$$-\frac{\partial}{\partial x}(\rho u) - \frac{\partial}{\partial y}(\rho v) - \frac{\partial}{\partial z}(\rho w) = -\nabla \cdot (\rho \mathbf{v})$$

By defintion ρ is the mass per unit volume , and so $\partial \rho / \partial t$ is the rate of increase of mass per unit volume. Hence, one form of the continuity equation is

$$\frac{\partial \rho}{\partial t} + \nabla \cdot (\rho \mathbf{v}) = 0. \tag{1.8}$$

Since we are only thinking of incompressible fluids, which are fluids whose density does not change in time we have

$$\frac{D\rho}{Dt} = \frac{\partial \rho}{\partial t} + \mathbf{v} \cdot \nabla \rho = 0, \tag{1.9}$$

and so the continuity equation is simply

$$\nabla \cdot \mathbf{v} = 0. \tag{1.10}$$

1.1.3 Shallow Water Equations

We shall now further simplify the momentum and continuity equation to apply to a body of water whose depth is small compared to another length scale, for instance the length of the river. This approximation is valid in many instances such as flow in open channels, the tides and waves breaking on a shallow beach. We will only be working in two dimensions, x which we shall take parallel to the undisturbed water surface and z which is vertically upwards. The velocity of the fluid will be given by $u(x, z, t)$ in the x-direction
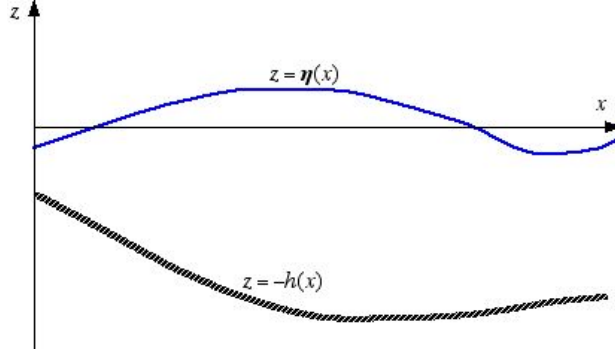
Figure 1.6: Schematic of coordinate system and variables used in the one dimensional shallow water equations.

and $w(x, z, t)$ in the z-direction. The lower boundary of the fluid is solid and will be taken to be $z = -h(x)$ so that the depth of the undisturbed water is h. The surface displacement is then given by $z = \eta(x, t)$. In two dimensions and ignoring the Coriolis effect on the basis that it will be negligible as we are looking at a small region, the momentum equations and continuity equation can written as

$$\frac{\partial u}{\partial t} + u \frac{\partial u}{\partial x} + w \frac{\partial u}{\partial z} = -\frac{1}{\rho} \frac{\partial p}{\partial x} \tag{1.11}$$

$$\frac{\partial w}{\partial t} + u \frac{\partial w}{\partial x} + w \frac{\partial w}{\partial z} = -\frac{1}{\rho} \frac{\partial p}{\partial z} - g \tag{1.12}$$

$$\frac{\partial u}{\partial x} + \frac{\partial w}{\partial z} = 0 \tag{1.13}$$

In addition to the above equations we also have boundary conditions. Along the bottom boundary of the fluid $z = -h(x)$ we must have zero vertical velocity, which can be expressed as

$$\frac{D}{Dt} (\eta + h) \Big|_{z=-h} = (w + u \, h_x) \Big|_{z=-h} = 0. \tag{1.14}$$

At the free surface we have a kinematic condition

$$\frac{D}{Dt} (\eta - z) \Big|_{z=\eta} = (\eta_t + u \, \eta_x - w) \Big|_{z=\eta} = 0. \tag{1.15}$$

and also the dynamical condition

$$p \Big|_{z=\eta} = 0. \tag{1.16}$$

Integrating the continuity equation (1.13) over the depth of the fluid we find

$$\int_{-h}^{\eta} u_x \, dz + w \Big|_{-h}^{\eta} = 0, \tag{1.17}$$

and with the use of (1.14) and (1.15) to substitute the values of w at $z = -h$ and $z = \eta$ respectively we obtain

$$\int_{-h}^{\eta} u_x \, dz + \eta_t + u \Big|_{\eta} \eta_x + u \Big|_{-h} h_x = 0. \tag{1.18}$$

6

With the use of the relation

$$\frac{\partial}{\partial x} \int_{-h(x)}^{\eta(x)} u \, dz = u\Big|_{z=\eta} \eta_x + u\Big|_{z=-h} h_x + \int_{-h}^{\eta} u_x \, dz$$

this simplifies to

$$\frac{\partial}{\partial x} \int_{-h}^{\eta} u \, dz + \eta_t = 0. \tag{1.19}$$

We now make the assumption that the the z-component of the fluid has negligible effect on the pressure, p. If we set the z-component of acceleration is negligible in comparison to the pressure gradient, this can be ignored and so integrating (1.12) over the vertical depth we have

$$0 = -\frac{1}{\rho} p\Big|_z^{\eta} - g\left(\eta - z\right). \tag{1.20}$$

Using boundary condition (1.16) we get the hydrostatic relation

$$p = \rho g \left(\eta - z\right). \tag{1.21}$$

From this we obtain

$$p_x = \rho g \eta_x, \tag{1.22}$$

which shows that p_x is independent of z. This means that, by (1.2), the acceleration in the x-direction is also independent of z and hence so is the velocity u in the x-direction if it is at any given time. We shall assume this to be the case, so that now $u = u(x,t)$ only depends on x and t and integrating over the depth results in

$$\int_{-h}^{\eta} u \, dz = u\left(\eta + h\right). \tag{1.23}$$

Using this relation in equation (1.19) results in the final form of the continuity equation under shallow water approximations

$$\eta_t + \left(u\left(\eta + h\right)\right)_x = 0. \tag{1.24}$$

Also, utilising the equation (1.22), the momentum equation (1.11) becomes

$$u_t + u\, u_x = -g\eta_x. \tag{1.25}$$

As shown in [20] we can rewrite the shallow water equations we have just derived in an alternate form by making use of the variable

$$c = \sqrt{g\left(\eta + h\right)} \tag{1.26}$$

which is the propagation speed of small disturbances in the fluid relative to the flow introduced before. From this we have

$$c_t = \frac{g\eta_t}{2c} \qquad\qquad c_x = \frac{g\eta_x + gh_x}{2c}$$

which allows us to rewrite (1.24) and (1.25) as

$$u_t + uu_x + 2cc_x - gh_x = 0 \tag{1.27}$$

$$2c_t + 2uc_x + cu_x = 0. \tag{1.28}$$

1.1.4 Method of Characteristics

If we take the case where the slope of the bottom boundary is constant, in other words

$$m \equiv gh_x = \text{constant}$$

then we easily find that addition of (1.27) and (1.28) yields

$$\left\{ \frac{\partial}{\partial t} + (u + c) \frac{\partial}{\partial x} \right\} \cdot (u + 2c - mt) = 0 \qquad (1.29)$$

while subtraction of (1.28) from (1.27) results in

$$\left\{ \frac{\partial}{\partial t} + (u - c) \frac{\partial}{\partial x} \right\} \cdot (u - 2c - mt) = 0. \qquad (1.30)$$

The first equation shows that the variable $u + 2c - mt$ is constant for a point moving through the fluid with velocity $u + c$, while the second states that $u - 2c - mt$ remains constant for a point moving through the fluid with velocity $u - c$. Another way to express this would be to say we have two sets of curves in the x, t plane, C_1 and C_2, which are known as characteristics and along these curves the associated functions are constant. In this case

$$\begin{array}{llll} C_1 : & \frac{dx}{dt} = u + c & \text{along which} & u + 2c - mt = k_1 = \text{constant} \\ C_2 : & \frac{dx}{dt} = u - c & \text{along which} & u - 2c - mt = k_2 = \text{constant} \end{array} \qquad (1.31)$$

The constants k_1 and k_2 will generally be different along different curves in the family of characteristics.
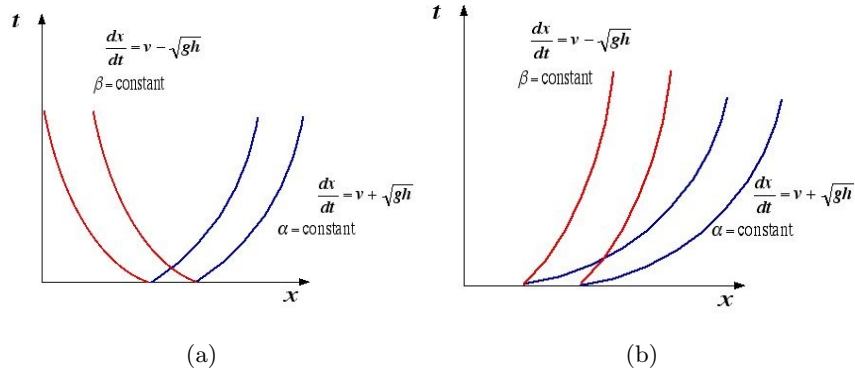
Figure 1.7: Diagrams showing the directions of characteristic curves for the case of (a) subcritical and (b) supercritical flows.

Earlier on we introduced the idea that a fluid could be supercritical or subcritical. We can use the idea of characteristics to visualise this. Suppose we have a fluid which has a positive flow velocity, $u > 0$. This would mean that the slope of the family of characteristics C_1 will always be positive. If we now assume that the fluid is supercritical we have $u - c > 0$ and so our family of characteristics C_2 also has a positive slope, see diag 1.7. However if we instead assume the flow to be subcritical then we have $u - c < 0$ and now the C_2 family of characteristics will slope to the left.

At a hydraulic jump there is a change in the fluid from supercritical flow to subcritical. Therefore the characteristics of the family C_2 will now intersect, see figure 1.8. Along the boundary of intersection there is a jump in values of u and c (or η) which is called a shock.
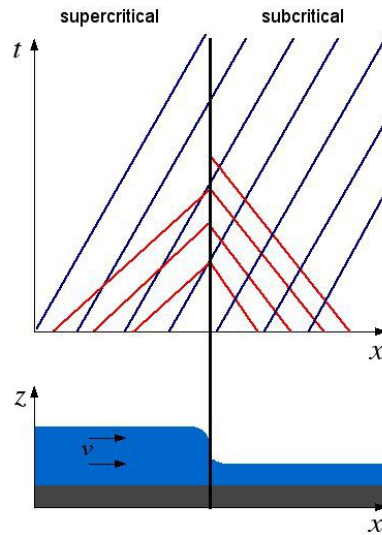
Figure 1.8: Illustration of how the characteristics intersect as the fluid flow changes from supercritical to subcritical causing a shock to form.

Chapter 2

The Finite Element Method

The finite element method is a combination of a finite-dimensional representation and a weak form of the differential equation to be solved. The term 'finite element' was first used by Clough (1960) [5], however the principles of the method had been around for at least 20 years by this time. It had developed from engineers performing stability analysis on aircraft in the 1940's. In 1943 Courant [6] used piecewise polynomial interpolation over triangular subregions to model torsion problems. By the 1960's the finite element method was being applied to problems in stress analysis, fluid flow, heat transfer and other areas and by the 1970's non-linear problems were also being solved with the method [4]. Today the finite element method is widely used in a range of different areas, from fluid flow and heat flux to deformation and stress analysis of buildings, bridges and aircraft and in meteorology and oceanography.

We shall now review three different forms of the finite element method which were investigated by White et al. [22]. In [22] the linearized shallow-water equations, with homogeneity in the y-direction, were solved in a finite domain taking the reference fluid depth h to be constant.

$$\frac{\partial u}{\partial t} - fv = -g\frac{\partial \eta}{\partial x},$$
$$\frac{\partial v}{\partial t} + fu = 0,$$
$$\frac{\partial \eta}{\partial t} + h\frac{\partial u}{\partial x} = 0,$$

where $f = 2\Omega\sin\phi$ is the Coriolis parameter, taken to be constant. We are working within the domain $x \in [-L/2, L/2]$ for some value L and $t > 0$ with boundary conditions $u(x = \pm L/2, t) = 0$.

These equations were then non-dimensionalized by taking the characteristic scales f^{-1}, L, η_0 and $Lh^{-1}f\eta_0$ for time, space, elevation and velocities

respectively to obtain

$$\frac{\partial u}{\partial t} - v = -\alpha^2 \frac{\partial \eta}{\partial x},$$

$$\frac{\partial v}{\partial t} + u = 0, \tag{2.1}$$

$$\frac{\partial \eta}{\partial t} + \frac{\partial u}{\partial x} = 0,$$

where $\alpha = \frac{\sqrt{gh}}{fL}$. Our domain is now $x \in [-1/2, 1/2]$ and $t > 0$ with boundary conditions $u(x = \pm 1/2, t) = 0$.

Two sets of initial conditions were investigated. The first was a motionless layer of fluid with a discontinuity in its elevation,

$$u(x, 0) = v(x, 0) = 0,$$

$$\eta(x, 0) = \begin{cases} -1 & if \quad -1/2 \leqslant x < 0, \\ 1 & if \quad 0 < x \leqslant 1/2. \end{cases} \tag{2.2}$$

The second is a generalization of this case using a hyperbolic tangent function to model the elevation to smooth the discontinuity,

$$u(x, 0) = v(x, 0) = 0,$$

$$\eta(x, 0) = \tanh(Rx). \tag{2.3}$$

The parameter R is used to alter how steep the change in elevation is, the larger the value taken for R the closer the function becomes to the initial discontinuity (2.2).

2.1 The Method of Characteristics

As the equations (2.1) are a system of first order hyperbolic equations they can be written in the form $\mathbf{A}\dfrac{\partial \mathbf{u}}{\partial t} + \mathbf{B}\dfrac{\partial \mathbf{u}}{\partial x} = \mathbf{d}$ as follows

$$\begin{pmatrix} 1 & 0 & 0 \\ 0 & 1 & 0 \\ 0 & 0 & 1 \end{pmatrix} \frac{\partial}{\partial t} \begin{pmatrix} u \\ v \\ \eta \end{pmatrix} + \begin{pmatrix} 0 & 0 & \alpha^2 \\ 0 & 0 & 0 \\ 1 & 0 & 0 \end{pmatrix} \frac{\partial}{\partial x} \begin{pmatrix} u \\ v \\ \eta \end{pmatrix} = \begin{pmatrix} v \\ -u \\ 0 \end{pmatrix}. \tag{2.4}$$

From this we can calculate the eigenvalues and corresponding eigenvectors and hence obtain a system of three ordinary differential equations,

$$\frac{d}{dt} v = -u \qquad \text{on } \frac{dx}{dt} = 0,$$

$$\frac{d}{dt} (\alpha \eta + u) = v \qquad \text{on } \frac{dx}{dt} = \alpha, \tag{2.5}$$

$$\frac{d}{dt} (\alpha \eta - u) = -v \qquad \text{on } \frac{dx}{dt} = -\alpha.$$

By dividing our domain into K intervals in space and N time intervals we can then use a simple finite difference method to solve these, provided we are within the Courant-Friedrich-Lewy condition which, as both space and
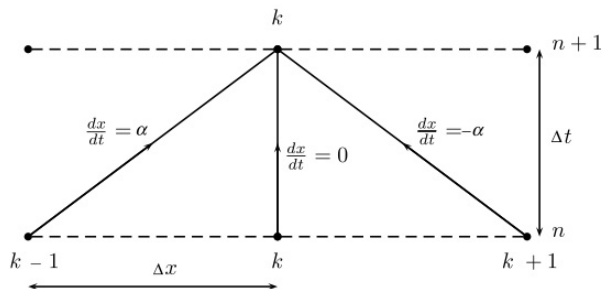
Figure 2.1: Figure showing the orientation of the characteristics and the space and time discretizations. (Diagram taken from [22].)

time intervals are dimensionless, is given by $\frac{\triangle t}{\triangle x} < \alpha$. Using the forward Euler scheme we have

$$\frac{v_k^{n+1} - v_k^n}{\triangle t} = -u_k^n,$$

$$\frac{\alpha \eta_k^{n+1} + u_k^{n+1} - \alpha \eta_k^n - u_k^n}{\triangle t} = v_{k-1}^n,$$

$$\frac{\alpha \eta_k^{n+1} - u_k^{n+1} - \alpha \eta_k^n + u_k^n}{\triangle t} = -v_{k+1}^n,$$

where $k = 1, \ldots, K + 1$ is the spatial discretization and $n = 1, \ldots, N + 1$ is the time discretization.

This method gives good results as long as the time integration is accurate enough, and a higher order method than the Euler method is required in practice. However characteristics cannot be calculated for all systems of partial differential equations, as they have been for (2.1). Even first order systems cannot be placed in matrix form if there are nonlinear terms present and so often this is not a viable option.

2.2 The Continuous Galerkin Method

This is the simplest form of the finite element method. We again divide our domain into K, not necessarily equal, intervals $[x_0, \ldots, x_j, x_{j+1}, \ldots, x_K]$. If we discretize our equations (2.1) in time, then multiply by a test function $\hat{\mathbf{u}} = (\hat{u}, \hat{v}, \hat{\eta})$, which are usually taken to be low order polynomials, and integrate over our domain Ω. we can then find $u^{n+1}, v^{n+1}, \eta^{n+1}$ such that

$$\int_\Omega \left(\frac{\eta^{n+1} - \eta^n}{\triangle t} \hat{\eta} + \frac{\partial u^n}{\partial x} \hat{\eta} \right) \, dx = 0,$$
$$\int_\Omega \left(\frac{u^{n+1} - u^n}{\triangle t} \hat{u} - v^n \hat{u} + \alpha^2 \frac{\partial \eta^{n+1}}{\partial x} \hat{u} \right) \, dx = 0, \qquad (2.6)$$
$$\int_\Omega \left(\frac{v^{n+1} - v^n}{\triangle t} \hat{v} + u^{n+1} \hat{v} \right) \, dx = 0,$$

12

for n odd, and

$$\int_\Omega \left(\frac{\eta^{n+1} - \eta^n}{\triangle t} \hat{\eta} + \frac{\partial u^n}{\partial x} \hat{\eta} \right) \, dx = 0,$$

$$\int_\Omega \left(\frac{v^{n+1} - v^n}{\triangle t} \hat{v} + u^n \hat{v} \right) \, dx = 0, \qquad (2.7)$$

$$\int_\Omega \left(\frac{u^{n+1} - u^n}{\triangle t} \hat{u} - v^{n+1} \hat{u} + \alpha^2 \frac{\partial \eta^{n+1}}{\partial x} \hat{u} \right) \, dx = 0,$$

for n even. This is a 'forward-backward' time-stepping scheme, where we first calculate η^{n+1} and then use this updated value in the equations to calcuate u^{n+1}, v^{n+1}. We alternate the order in which u^{n+1} and v^{n+1} are calculated so the Coriolis term is semi-implicit, which ensures that no energy is artificially created or dissipated by this term. We then replace each variable u, v, η in the above equations by the discrete approximations given by

$$a^{n+1} \simeq a_h^{n+1} = \sum_{j=0}^{K} A_j^{n+1} \phi_j(x), \qquad (2.8)$$

where A_j^{n+1} are the values of the variables at node j and time step $n + 1$. The basis functions ϕ_j are piecewise linear and are defined by

$$\phi_0(x) = \frac{x_1 - x}{x_1 - x_0} \qquad x_0 \leqslant x \leqslant x_1$$

$$\phi_j(x) = \begin{cases} \frac{x - x_{j-1}}{x_j - x_{j-1}} & x_{j-1} \leqslant x \leqslant x_j \\ \\ \frac{x_{j+1} - x}{x_{j+1} - x_j} & x_j \leqslant x \leqslant x_{j+1} \end{cases} \qquad j = 1, \ldots, K - 1.$$

$$\phi_K(x) = \frac{x - x_{K-1}}{x_K - x_{K-1}} \qquad x_{K-1} \leqslant x \leqslant x_K \qquad (2.9)$$

Similarly we approximate our test functions $\hat{\mathbf{u}}$ by $\phi_j(x), j = 1, \ldots, K$. Therefore both $\mathbf{u}_h$ and $\hat{\mathbf{u}}_h$ are continuous over our domain Ω and piecewise linear over each element.

Using this method to solve (2.1) with an initial discontinuous elevation (2.2), White et al. [22] found that spurious oscillations were produced no matter how fine a mesh was used. However these oscillations were less pronounced when a smoother initial elevation (2.3) was used. This would suggest that this method would not be very effective when used to model problems whose variables have steep gradients in their solution or initial condition.

2.3 The Discontinuous Galerkin Method

In this method the approximated functions $\mathbf{u}_h$ do not have to be continuous across node boundaries. This is because two computational nodes are now associated with one physical node, representing the values of the variable to the left and right of the node, see figure 2.2. This is ideal for modelling variables which have steep gradients and discontinuities. However we still

13
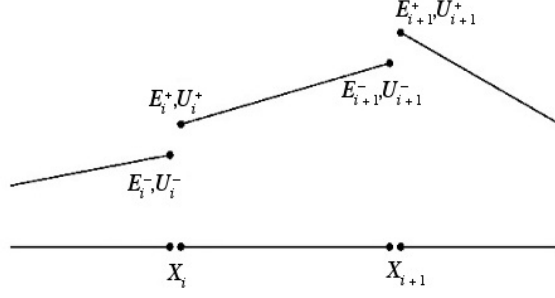
Figure 2.2: Discontinuity of variables at element boundaries.

need to ensure information can be passed from one element to another. Therefore an extra term must be added to the weak formulation derived for the continuous Galerkin method which enforces a weak continuity over u and η. For the backward-forward scheme we have

$$\sum_{e=1}^{K} \int_{\Omega_e} \left(\frac{\eta^{n+1} - \eta^n}{\triangle t} \hat{\eta} + \frac{\partial u^n}{\partial x} \hat{\eta} \right) \, dx + \sum_{e=1}^{K} |a(\hat{\eta}) \, [u^n]|_{\partial\Omega_e} = 0,$$

$$\sum_{e=1}^{K} \int_{\Omega_e} \left(\frac{u^{n+1} - u^n}{\triangle t} \hat{u} - v^n \hat{u} + \alpha^2 \frac{\partial \eta^{n+1}}{\partial x} \hat{u} \right) \, dx$$

$$+ \sum_{e=1}^{K} \left| a(\hat{u}) \left[\alpha^2 \eta^{n+1} \right] \right|_{\partial\Omega_e} = 0,$$

$$\sum_{e=1}^{K} \int_{\Omega_e} \left(\frac{v^{n+1} - v^n}{\triangle t} \hat{v} + u^{n+1} \hat{v} \right) \, dx = 0, \qquad (2.10)$$

for n odd, and

$$\sum_{e=1}^{K} \int_{\Omega_e} \left(\frac{\eta^{n+1} - \eta^n}{\triangle t} \hat{\eta} + \frac{\partial u^n}{\partial x} \hat{\eta} \right) \, dx + \sum_{e=1}^{K} |a(\hat{\eta}) \, [u^n]|_{\partial\Omega_e} = 0,$$

$$\sum_{e=1}^{K} \int_{\Omega_e} \left(\frac{v^{n+1} - v^n}{\triangle t} \hat{v} + u^n \hat{v} \right) \, dx = 0, \qquad (2.11)$$

$$\sum_{e=1}^{K} \int_{\Omega_e} \left(\frac{u^{n+1} - u^n}{\triangle t} \hat{u} - v^{n+1} + v^n \hat{u} + \alpha^2 \frac{\partial \eta^{n+1}}{\partial x} \hat{u} \right) \, dx$$

$$+ \sum_{e=1}^{K} \left| a(\hat{u}) \left[\alpha^2 \eta^{n+1} \right] \right|_{\partial\Omega_e} = 0,$$

for n even. The additional terms in (2.10)-(2.11) are to enforce a weak continuity in u and η across element boundaries. The vertical bars indicate

14

that the expression is to be evaluated over the boundaries of each element and $[u^n(X_i)] = U_i^- - U_i^+$ is the jump of the variable across node i. The function $a(\hat{u})$ is defined as

$$a(\hat{u}) = \left(\lambda - \frac{1}{2}\text{sign}(\hat{n})\right)\hat{u},$$

where $\hat{n}$ is the outward pointing normal along each element boundary and $\lambda \in [-1/2, 1/2]$ is a parameter to alter the weight given to the jump. Taking $\lambda = 0$ gives a centred scheme, however if it is known in which direction each variable is travelling in a given problem then more weight is given to the respective node, i^- for left-ward moving variables and i^+ for variables moving to the right.

The system (2.10)-(2.11) can be rearranged using integration by parts, as Hanert et al. [12] has shown, to become

$$\sum_{e=1}^{K}\int_{\Omega_e}\left(\frac{\eta^{n+1}-\eta^n}{\triangle t}\hat{\eta} + \frac{\partial u^n}{\partial x}\hat{\eta}\right)dx$$

$$+\sum_{i=1}^{K+1}\left(\left(\frac{1}{2}+\lambda\right)u^n(X_i^-) + \left(\frac{1}{2}-\lambda\right)u^n(X_i^+)\right)\left(\hat{\eta}(X_i^-) - \hat{\eta}(X_i^+)\right) = 0,$$

$$\sum_{e=1}^{K}\int_{\Omega_e}\left(\frac{u^{n+1}-u^n}{\triangle t}\hat{u} - v^n\hat{u} + \alpha^2\eta^{n+1}\frac{\partial\hat{u}}{\partial x}\right)dx$$

$$+\alpha^2\sum_{i=1}^{K+1}\left(\left(\frac{1}{2}+\lambda\right)\eta^{n+1}(X_i^-) + \left(\frac{1}{2}-\lambda\right)\eta^{n+1}(X_i^+)\right)\left(\hat{u}(X_i^-) - \hat{u}(X_i^+)\right) = 0,$$

$$\sum_{e=1}^{K}\int_{\Omega_e}\left(\frac{v^{n+1}-v^n}{\triangle t}\hat{v} + u^{n+1}\hat{v}\right)dx = 0,$$

for n odd, and

$$\sum_{e=1}^{K}\int_{\Omega_e}\left(\frac{\eta^{n+1}-\eta^n}{\triangle t}\hat{\eta} + \frac{\partial u^n}{\partial x}\hat{\eta}\right)dx$$

$$+\sum_{i=1}^{K+1}\left(\left(\frac{1}{2}+\lambda\right)u^n(X_i^-) + \left(\frac{1}{2}-\lambda\right)u^n(X_i^+)\right)\left(\hat{\eta}(X_i^-) - \hat{\eta}(X_i^+)\right) = 0,$$

$$\sum_{e=1}^{K}\int_{\Omega_e}\left(\frac{v^{n+1}-v^n}{\triangle t}\hat{v} + u^n\hat{v}\right)dx = 0,$$

$$\sum_{e=1}^{K}\int_{\Omega_e}\left(\frac{u^{n+1}-u^n}{\triangle t}\hat{u} - v^{n+1}\hat{u} + \alpha^2\eta^{n+1}\frac{\partial\hat{u}}{\partial x}\right)dx$$

$$+\alpha^2\sum_{i=1}^{K+1}\left(\left(\frac{1}{2}+\lambda\right)\eta^{n+1}(X_i^-) + \left(\frac{1}{2}-\lambda\right)\eta^{n+1}(X_i^+)\right)\left(\hat{u}(X_i^-) - \hat{u}(X_i^+)\right) = 0,$$

for n even.

White et al. again experimented using this method on the initial discontinuous elevation (2.2) and the smoother initial condition (2.3). Rather surprisingly, results were less accurate than those obtained with the continuous Galerkin method, with severe spurious oscillations occurring from the step-like discontinuity regardless of element width or the value taken for λ. The centred scheme, with $\lambda = 0$, in fact produced the least oscillations suggesting that symmetry is important in this problem.

When the hyperbolic tangent function was used for the initial elevation the frequency of the oscillations was less pronounced and increasing the number of elements reduced them further. However the continuous Galerkin method still outperformed this scheme by far, especially for smoother initial conditions (lower value for R).

This would suggest that forcing weak continuity of u, η does not help in improving the method and so thought must be given as to what other variables continuity can be imposed upon.

2.4   The Discontinuous Riemann Galerkin Method

It is suggested that as characteristic variables carry information along characteristic curves, enforcing continuity of these variables between elements may be of more use. We are also able to apply appropriate weighting as we know the direction of propagation for each characteristic variable. This is known as a discontinuous Galerkin finite element method with a Riemann solver as we are imposing continuity of the Riemann variables.

As before we have a variational formulation similar to (2.6)-(2.7) but with extra terms for the continuity of the characteristic variables

$$\sum_{e=1}^{K} \int_{\Omega_e} \left(\frac{\eta^{n+1} - \eta^n}{\triangle t} \hat{\eta} + \frac{\partial u^n}{\partial x} \hat{\eta} \right) \, dx$$

$$+ \sum_{e=1}^{K} |a(\hat{\eta}) \left[\alpha \eta^n + u^n \right]|_{\partial \Omega_e} + \sum_{e=1}^{K} |b(\hat{\eta}) \left[\alpha \eta^n - u^n \right]|_{\partial \Omega_e} = 0,$$

$$\sum_{e=1}^{K} \int_{\Omega_e} \left(\frac{u^{n+1} - u^n}{\triangle t} \hat{u} - v^n \hat{u} + \alpha^2 \frac{\partial \eta^{n+1}}{\partial x} \hat{u} \right) \, dx$$

$$+ \sum_{e=1}^{K} \left| a(\hat{u}) \left[\alpha u^n + \alpha^2 \eta^{n+1} \right] \right|_{\partial \Omega_e} + \sum_{e=1}^{K} \left| b(\hat{u}) \left[\alpha u^n - \alpha^2 \eta^{n+1} \right] \right|_{\partial \Omega_e} = 0,$$

$$\sum_{e=1}^{K} \int_{\Omega_e} \left(\frac{v^{n+1} - v^n}{\triangle t} \hat{v} + u^{n+1} \hat{v} \right) \, dx = 0, \qquad (2.12)$$

for n odd, and

$$\sum_{e=1}^{K} \int_{\Omega_e} \left(\frac{\eta^{n+1} - \eta^n}{\triangle t} \hat{\eta} + \frac{\partial u^n}{\partial x} \hat{\eta} \right) dx$$

$$+ \sum_{e=1}^{K} \left| a(\hat{\eta}) \left[\alpha \eta^n + u^n \right] \right|_{\partial \Omega_e} + \sum_{e=1}^{K} \left| b(\hat{\eta}) \left[\alpha \eta^n - u^n \right] \right|_{\partial \Omega_e} = 0,$$

$$\sum_{e=1}^{K} \int_{\Omega_e} \left(\frac{v^{n+1} - v^n}{\triangle t} \hat{v} + u^n \hat{v} \right) dx = 0, \qquad (2.13)$$

$$\sum_{e=1}^{K} \int_{\Omega_e} \left(\frac{u^{n+1} - u^n}{\triangle t} \hat{u} - v^{n+1} \hat{u} + \alpha^2 \frac{\partial \eta^{n+1}}{\partial x} \hat{u} \right) dx$$

$$+ \sum_{e=1}^{K} \left| a(\hat{u}) \left[\alpha u^n + \alpha^2 \eta^{n+1} \right] \right|_{\partial \Omega_e} + \sum_{e=1}^{K} \left| b(\hat{u}) \left[\alpha u^n - \alpha^2 \eta^{n+1} \right] \right|_{\partial \Omega_e} = 0,$$

for n even, where

$$a(\hat{u}) = \frac{1}{2} \left(\frac{1}{2} - \lambda \text{sign}(\hat{n}) \right) \hat{u}, \qquad b(\hat{u}) = \frac{1}{2} \left(\frac{1}{2} + \lambda \text{sign}(\hat{n}) \right) \hat{u}.$$

Again we can rearrange (2.12)-(2.13) by integrating by parts and taking $\lambda = 1/2$ we obtain

$$\sum_{e=1}^{K} \int_{\Omega_e} \left(\frac{\eta^{n+1} - \eta^n}{\triangle t} \hat{\eta} + \frac{\partial u^n}{\partial x} \hat{\eta} \right) dx$$

$$+ \frac{1}{2} \sum_{i=1}^{K+1} [\hat{\eta}(X_i)] \left\{ (\alpha \eta^n(X_i^-) + u^n(X_i^-)) - (\alpha \eta^n(X_i^+) - u^n(X_i^+)) \right\} = 0,$$

$$\sum_{e=1}^{K} \int_{\Omega_e} \left(\frac{u^{n+1} - u^n}{\triangle t} \hat{u} - v^n \hat{u} + \alpha^2 \eta^{n+1} \frac{\partial \hat{u}}{\partial x} \right) dx$$

$$+ \frac{1}{2} \alpha \sum_{i=1}^{K+1} [\hat{u}(X_i)] \left\{ (\alpha \eta^{n+1}(X_i^-) + u^n(X_i^-)) + (\alpha \eta^{n+1}(X_i^+) - u^n(X_i^+)) \right\} = 0,$$

$$\sum_{e=1}^{K} \int_{\Omega_e} \left(\frac{v^{n+1} - v^n}{\triangle t} \hat{v} + u^{n+1} \hat{v} \right) dx = 0,$$

for n odd, and

$$\sum_{e=1}^{K} \int_{\Omega_e} \left(\frac{\eta^{n+1} - \eta^n}{\triangle t} \hat{\eta} + \frac{\partial u^n}{\partial x} \hat{\eta} \right) dx$$

$$+ \frac{1}{2} \sum_{i=1}^{K+1} [\hat{\eta}(X_i)] \left\{ (\alpha \eta^n(X_i^-) + u^n(X_i^-)) - (\alpha \eta^n(X_i^+) - u^n(X_i^+)) \right\} = 0,$$

$$\sum_{e=1}^{K} \int_{\Omega_e} \left(\frac{v^{n+1} - v^n}{\triangle t} \hat{v} + u^n \hat{v} \right) \, dx = 0,$$

$$\sum_{e=1}^{K} \int_{\Omega_e} \left(\frac{u^{n+1} - u^n}{\triangle t} \hat{u} - v^{n+1} \hat{u} + \alpha^2 \eta^{n+1} \frac{\partial \hat{u}}{\partial x} \right) \, dx$$

$$+ \frac{1}{2} \alpha \sum_{i=1}^{K+1} [\hat{u}(X_i)] \left\{ (\alpha \eta^{n+1}(X_i^-) + u^n(X_i^-)) + (\alpha \eta^{n+1}(X_i^+) - u^n(X_i^+)) \right\} = 0,$$

for n even.

This scheme was applied to the problem with initial discontinuous elevation (2.2) and produced no spurious oscillations, even on a coarse mesh. As the initial condition was smoothed using (2.3) the L_2 norm of the error became smaller, becoming of the order of $10^{-3.5}$ when $R = 1$.

The methods were all compared by measuring the L_2 norm of the error as the steepness of the initial conditions was altered. The discontinuous Riemann-Galerkin method (DRGM) consistently outperformed the discontinuous Galerkin method (DGM). For fairly smooth initial conditions, taking $R = 1$ the continuous method had roughly the same error as the DRGM. However when the error over a restricted domain containing no discontinuities was computed, the DRGM was twice as accurate than the continuous method. This suggests that spurious oscillations which occur from the continuous method spread into areas where the solution is smooth and affects the accuracy over a wider area than the DRGM. However extension of the DRGM to higher dimensions would be difficult, as calculating the Riemann variables is not usually simple.

Chapter 3

Adaptive Mesh Techniques

The reasoning behind moving a mesh over time is in order to efficiently capture features which are very localised. For instance we may have a solution which is very stable over most of the domain but in a few localised areas there are moving features which require a high resolution mesh in order to accurately capture the solution. Also problems which have steep gradients need a high resolution around the slope, as if the mesh is too coarse the change in the solution becomes spread out over the element and so the gradient is not accurately represented.

In the particular area of measuring discontinuties in flow problems, initially shock fitting techniques were used [14]. This is where two separate solutions were obtained either side of where the shock is computed to be and are then pieced together again. Now it is more common to use a shock capturing technique, where the discontinuity is automatically formed, as in most problems the position of the discontinuity is not explicitly known, for example in [9].

Some of the earliest attempts at constructing an adaptive mesh involved taking a time derivative of the governing equations of the coordinate mapping [13] and grid sizes were related to derivatives of flow variables [8]. Later, systems which simultaneously solve a physical equation and a grid equation were investigated in Rai & Anderson[19].

There are three general types of mesh adaptation. The first type is known as h-refinement and adds extra nodes to the areas where the solution is badly approximated. Secondly, p-refinement increases the order of the numerical approximation, being used to improve the local accuracy of the solution. The third is known as r-refinement which dynamically moves a fixed number of nodes to the most effective location. Combinations of these three types are also used, for instance hr-refinement where nodes are moved and also added where needed. They all need a solution indicator to determine where adaptation is needed. Ideally the solution indicators would be based on error estimators, however this is rarely done in practice as the exact solution is not known.

The r-refinement is simple to implement in theory as nodes are not generated nor taken away over time. The grid should also naturally move to fit the most prominent feature of the problem. It is these methods we shall focus on.

3.1 Moving Mesh Methods

An adaptive mesh is often generated by taking a mapping $x(\xi)$ from a regularly structured grid in computational space Ω_C to a grid in physical space Ω. By altering the mapping we can alter the location of the nodes in physical space and even the boundaries of the domain. There are two main groups
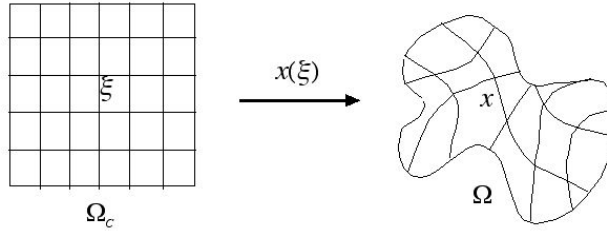

Figure 3.1: The computational grid (left) and the transformation to the computational domain (right).

which can be classified under r-refinement. The first are the location-based methods. These directly control where the physical nodes are to be located at each time step and interpolate the solution from the old mesh to the new mesh. In other words this affects the mapping $x(\xi)$ directly, which becomes a function of time. The second group are velocity-based methods which assign a speed to each individual node at each time, in effect altering the time derivative of the mapping, $x_t(\xi)$. The velocities can be derived in various ways. A conservation principle can be imposed on an element, for instance conservation of mass, and from this a velocity is derived, or velocities can be taken from an external source, such as the discontinuity in the solution at each node.

3.1.1 Location based methods

The Method of Equidistribution

A location-based method uses the idea of equidistribution of some variable. Suppose we want to equally space the value of the function $M(x)$ over our physical domain. This is known as our monitor function. In one dimension we can take our computational nodes to be ξ_j such that $0 \leqslant \xi_j \leqslant 1$ and our physical nodes to be x_j such that $a \leqslant x_j \leqslant b$, then we have

$$\xi = \frac{\int_a^x M(\tilde{x})d\tilde{x}}{\int_a^b M(\tilde{x})d\tilde{x}}.$$

If we differentiate this twice with respect to ξ then we have

$$\frac{\partial}{\partial \xi}\left(M(x)\frac{\partial x}{\partial \xi}\right) = 0 \tag{3.1}$$

which can be solved for the map $x(\xi)$.

A commonly used monitor function is the arc length

$$M(x) = \sqrt{1 + \gamma \left(\frac{du}{dx}\right)^2} \tag{3.2}$$

where u is the function we are modelling and γ is a parameter which can be used to reduce the extent that the slope is used.

3.1.2 Velocity-based methods

The Lagrangian method

One of the simplest velocity based approaches is to use a Lagrangian co-ordinate system. This is constructed from the principle that we follow a single particle in the fluid. If the fluid has velocity $u(x,t)$, ξ is the reference parameter of the particle and $x(\xi, t)$ is the position of the particle at time t. Then the Lagrangian coordinate system moves with velocity

$$\frac{dx}{dt} = u.$$

However Lagrangian coordinate systems are very rarely used in numerical approximations due to the fact they produce a mesh which is very skew and liable to tangle.

Moving Finite Elements

This method was developed by Miller and Miller [16], [17] and is based on minimising the residual from the finite element formulation. Suppose we have a general time-dependent problem

$$\frac{\partial u}{\partial t} = \mathcal{L}u$$

where $\mathcal{L}$ is a spatial differential operator. The continuous moving finite element (MFE) method seeks to minimise the L_2 norm of the residual,

$$\min_{\mathbf{x}_t, \frac{Du}{Dt}} I_{mfe}\left[\mathbf{x}_t, \frac{Du}{Dt}\right] = \int \left(\frac{\partial u}{\partial t} - \mathcal{L}u\right)^2 W d\mathbf{x},$$

$$= \int \left(\frac{Du}{Dt} - \bigtriangledown u \cdot x_t - \mathcal{L}u\right)^2 W d\mathbf{x},$$

where W is a weight function and $\frac{Du}{Dt}$ is the material time derivative for ξ fixed. For the classical MFE method the weight function is taken as unity, $W = 1$, and for the gradient-weighted MFE method the weight function is $W = \frac{1}{1+|\bigtriangledown u|^2}$. By using this method there is a greater chance that the weighted L_2 norm of the residual will be close to its minimum, i.e. the solution will be as accurate as possible. However these equations can become degenerate and so extra care has to be taken.

The Conservation Principle

This is a commonly used velocity based method which computes nodal velocities by imposing a conservation principle on each element in physical space. Suppose we want to ensure each element conserved the variable M

$$\frac{d}{dt} \int_{a(t)}^{b(t)} M dx = 0,$$
(3.3)

which, using the Liebnitz integral rule, can be written as

$$\int_{a(t)}^{b(t)} \frac{\partial M}{\partial t} dx + \left[\frac{dx}{dt} M \right]_{a(t)}^{b(t)} = 0.$$
(3.4)

From this the mesh velocity dx/dt can be computed.

3.2 Methods to be Investigated

In my work I shall focus on two of these methods, namely the method of equidistribution and the conservation principle, which I shall now describe in more detail. I will apply these to two existing models. The first is a simple model based on the shallow water equations investigated by Kuo and Polvani [15] and the second is a more realistic model which simulates tidal flows in the Daly River in Australia. These shall be described in more detail later.

3.2.1 Method of Equidistribution

As the problem to be modelled requires a concentration of nodes in areas where the gradient of the water is large I shall use the arc length monitor function applied to the elevation η for equidistribution

$$M(x) = \sqrt{1 + \gamma \left(\frac{d\eta}{dx} \right)^2}.$$
(3.5)

As shown in [1], we can then solve (3.1) by an iterative process until the solution converges by using the algorithm

$$\frac{\partial}{\partial \xi} \left(M(x^p) \frac{\partial x^{p+1}}{\partial \xi} \right) = 0,$$
(3.6)

for $p = 0, 1, \ldots$ with $x^0 = \xi$, which can be discretized as

$$M(x_j^p) \left(x_{j+1}^{p+1} - x_j^{p+1} \right) - M(x_{j-1}^p) \left(x_j^{p+1} - x_{j-1}^{p+1} \right).$$
(3.7)

This can be written as the matrix system

$$T(\mathbf{x}^p) \mathbf{x}^{p+1} = \mathbf{b}$$
(3.8)

where

$$T(\mathbf{x}) = \begin{pmatrix} 1 & M(x_1) & 0 & \cdots & 0 \\ M(x_1) & -M(x_1) - M(x_2) & M(x_2) & \cdots & 0 \\ \vdots & \ddots & \ddots & \ddots & \vdots \\ 0 & \cdots & \ddots & \ddots & M(x_{N-1}) \\ 0 & \cdots & 0 & 0 & 1 \end{pmatrix}$$

and

$$\mathbf{b} = \begin{pmatrix} a \\ 0 \\ \vdots \\ 0 \\ b \end{pmatrix}$$

as the boundary of the domain is fixed. This iterative process can be carried out for every set number of time steps as the model is run.

We therefore now have a new grid, and so we need to interpolate the values of our variables onto our new node locations, which can be done in a number of ways.

3.2.2 The Conservation Principle

We shall impose the conservation of volume on each mesh element. This is given by

$$\frac{d}{dt} \int_{a(t)}^{b(t)} (\eta + h) \, dx = \int_{a(t)}^{b(t)} \frac{\partial}{\partial t} (\eta + h) \, dx + \left[\frac{dx}{dt} (\eta + h) \right]_{a(t)}^{b(t)} = 0, \quad (3.9)$$

where $a(t)$, $b(t)$ are the boundaries of the mesh element which move with time. From the continuity equation (1.24) we have

$$\frac{\partial}{\partial t} (\eta + h) = \frac{\partial}{\partial t} \eta = -\frac{\partial}{\partial x} (u (\eta + h))$$

and so (3.9) becomes

$$0 = \int_{a(t)}^{b(t)} \frac{\partial}{\partial x} (u (\eta + h)) \, dx + \left[\frac{dx}{dt} (\eta + h) \right]_{a(t)}^{b(t)} \quad (3.10)$$

$$= \left[-u (\eta + h) \right]_{a(t)}^{b(t)} + \left[\frac{dx}{dt} (\eta + h) \right]_{a(t)}^{b(t)}. \quad (3.11)$$

By rearrangement this then gives us a relation between the velocities of the nodes either side of the element

$$\dot{b} = u(b) - \frac{\eta(a) + h(a)}{\eta(b) + h(b)} (u(a) - \dot{a}) \quad (3.12)$$

where the dot represents the derivative with time, i.e. $\dot{b} = \frac{db}{dt}$, the node velocity at $x = b$. Therefore if we fix one end of the domain, say the left, we can compute the velocity at each node using (3.12).

Chapter 4

Numerical Results from the Basic Model

4.1 A Basic Numerical Model

Kuo and Polvani [15] investigated the geostrophic adjustment problem using the non-dimensionalized, one-dimensional, non-linear shallow water equations with rotation. They worked in a domain which had a flat bottom and so the depth of the undisturbed water h is constant. We used these equations, setting rotation to zero as we do not expect it to have a significant effect on our problem. The continuity and momentum equations are

$$\frac{\partial u}{\partial t} + \alpha u \frac{\partial u}{\partial x} + \frac{\partial \eta}{\partial x} = 0, \tag{4.1}$$

$$\frac{\partial \eta}{\partial t} + \frac{\partial u}{\partial x} + \alpha \frac{\partial}{\partial x} (\eta u) = 0, \tag{4.2}$$

where $\alpha = \eta_0/h$ is a scaling parameter which can be changed to adjust the extent of non-linearity in the equations, we shall be taking $\alpha = 0.4$ for our investigations. For a detailed analysis of the effect α has on the system refer to Kuo and Polvani [15].

These equations were used in a discontinuous finite element numerical model with linear basis functions as given in (2.9) which uses the second order Runge Kutta method for time integration, in a finite domain, $x \in [-15, 15]$, giving $u|_{(x=\pm 15)} = 0$.

We then adapted this method to allow the mesh to move, using the two methods in the previous chapter and investigated their effectiveness at modelling different initial conditions.

4.2 Method of equilibrium

To implement the method descibed in section 3.2.1 we adapted the mesh every 100 time steps as the code was run and, taking $\gamma = 1$, we then interpolated our elevation and velocity values to the new mesh nodes using piecewise cubic Hermite interpolation.

24

In figure 4.5 is a time series of the elevation from an initial condition of

$$\eta(x,0) = -\arctan(5x). \tag{4.3}$$

We have used 200 elements and 2000 time steps. As can be seen in figure 4.5 this method is very good at increasing the density of the nodes around the location of the shock.

4.3 Volume conservation

We have fixed the left hand boundary, $x = -15$, and used equation (3.12) to calculate the velocity associated with each subsequent node to the right. Note that, as we are working in a domain with a flat lower boundary, $h \equiv 0$ everywhere due to the scaled equations. Therefore the equation becomes

$$\dot{b} = u(b) - \frac{\eta(a)}{\eta(b)}\left(u(a) - \dot{a}\right). \tag{4.4}$$

As our grid is now moving during each time step we have to adapt our equations (4.1)-(4.2) to account for this. As shown in Baines et al. [2], if we have a fixed coordinate system $\mathbf{a}$ and a moving coordinate system $\mathbf{x}$, then we can define a mapping between these by

$$\mathbf{x} = \hat{\mathbf{x}}(\mathbf{a}, t).$$

If $\hat{u}(\mathbf{a}, t)$ is a variable measured from the fixed coordinate system, then its derivative is given by

$$\frac{\partial \hat{u}}{\partial t} = \frac{\partial u}{\partial t} + \frac{\partial \hat{\mathbf{x}}}{\partial t} \cdot \nabla u,$$

where $u(\mathbf{x}, t)$ is the same variable measured from the moving coordinate system. Therefore a general partial differential equation of the form

$$\frac{\partial u}{\partial t} = \mathcal{L}u,$$

where $\mathcal{L}$ is a spatial differential operator, can now be expressed in integral form in a moving mesh as

$$\frac{d}{dt}\int \hat{u}\,dx - \int \frac{\partial}{\partial x}\left(\hat{u}\frac{\partial \hat{x}}{\partial t}\right)\,dx = \int \mathcal{L}u\,dx.$$

Our equations (4.1)-(4.2) thus can be written

$$\frac{d}{dt}\int \hat{u}\,dx - \int \frac{\partial}{\partial x}\left(\hat{u}\frac{\partial \hat{x}}{\partial t}\right)\,dx + \int \left(\alpha u\frac{\partial u}{\partial x} + \frac{\partial \eta}{\partial x}\right)\,dx = 0, \tag{4.5}$$

$$\frac{d}{dt}\int \hat{\eta}\,dx - \int \frac{\partial}{\partial x}\left(\hat{\eta}\frac{\partial \hat{x}}{\partial t}\right)\,dx + \int \left(\frac{\partial u}{\partial x} + \alpha\frac{\partial}{\partial x}(\eta u)\right)\,dx = 0. \tag{4.6}$$

4.4 Comparison of the methods

We have again produced a time series of the elevation at $t = 0, 1, 2, 3, 4, 5$ using 200 elements and 2000 time steps from initial condition (4.3) for the volume conservation method and this is shown in figure 4.6. We can see that, although this method models the discontinuity very clearly, the water level is totally disproportionate when compared against the high resolution model, see figure 4.4. Unlike with the arc length model, the high density patch of nodes seem to centre just behind the shock which accounts for such a well-defined discontinuity.

(a) Methods used 50 elements and a time step of 0.01.

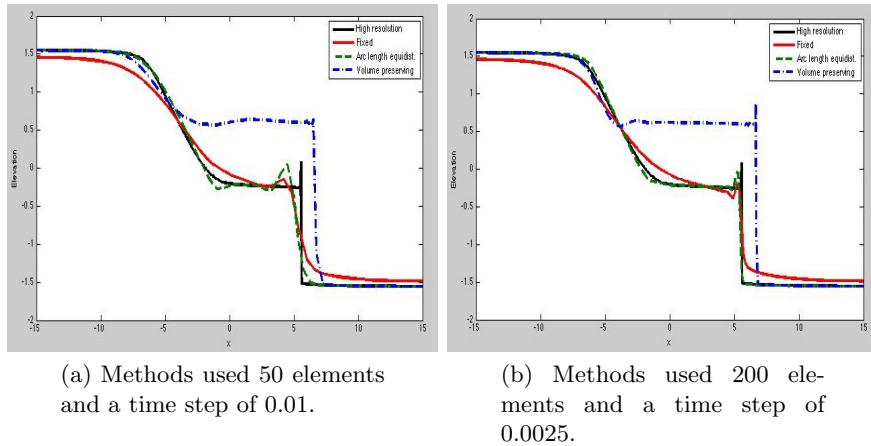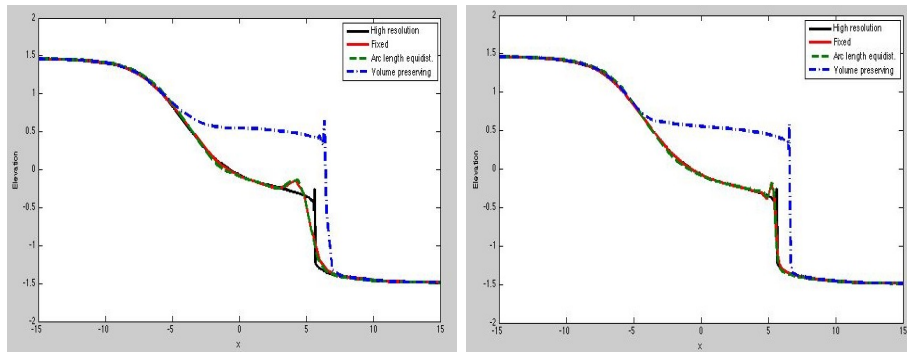(b) Methods used 200 elements and a time step of 0.0025.

Figure 4.1: Results computed by conserving the element volume, equidistributing arc length of η and a fixed mesh from initial condition $\eta(x, 0) = -\arctan(5x)$. These are compared to a high resolution solution computed on a fixed mesh with 2000 elements and a time step of 0.00025.

From figure 4.1 we see that the volume conservation method tends to overestimate the height of the discontinuity and the shock also seems to travel at a faster velocity, making it highly inaccurate overall. There is little difference between the arc length and fixed mesh methods, no matter what size elements are taken. However, the arc length method tends to fit the solution better overall, although it oscillates slightly more than the fixed mesh solution around the discontinuity.

I also looked at the effect different initial conditions had on the methods. With a smoother initial condition, see figure 4.2, the solution by the arc length method and the fixed grid became even more similar, while the volume conserving method still overemphasized the shock. A totally discontinuous initial condition provided some interesting results, as can be seen in figure 4.3. On this occasion the volume conserving method does not seem to have as big an error as before, and the shock is almost in the correct position as given by the high resolution solution. Again the arc length and fixed mesh methods produced almost identical results, both very close to what is thought to be the true solution. With the discontinuous initial condition both of these methods produce slight oscillations around the discontinuity, however the arc length method seems to produce a slightly lower frequency

(a) Methods used 50 elements and a time step of 0.01.

(b) Methods used 200 elements and a time step of 0.0025.

Figure 4.2: Results computed by conserving the element volume, equidistributing arc length of η and a fixed mesh from initial condition $\eta(x,0) = -\arctan(x)$. These are compared to a high resolution solution computed on a fixed mesh with 2000 elements and a time step of 0.00025.
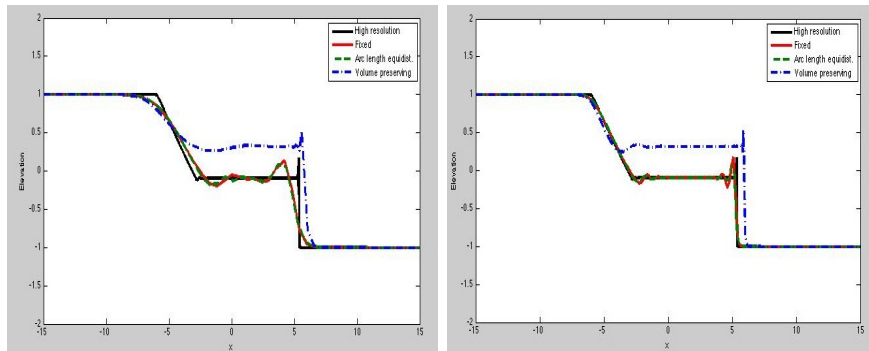
(a) Methods used 50 elements and a time step of 0.01.

(b) Methods used 200 elements and a time step of 0.0025.

Figure 4.3: Results computed by conserving the element volume, equidistributing arc length of η and a fixed mesh from initial condition $\eta(x,0) = 1$ for $x < 0$, and $\eta(x,0) = -1$ for $x > 0$. These are compared to a high resolution solution computed on a fixed mesh with 2000 elements and a time step of 0.00025.

of these.

Overall the arc length method produced at least as accurate results as the fixed mesh, although more investigation could be carried out on more complex problems to see if there is a distinct advantage over the fixed grid. The volume conserving method seems to perform better at capturing discontinuities clearly but the solution was highly inaccurate overall.
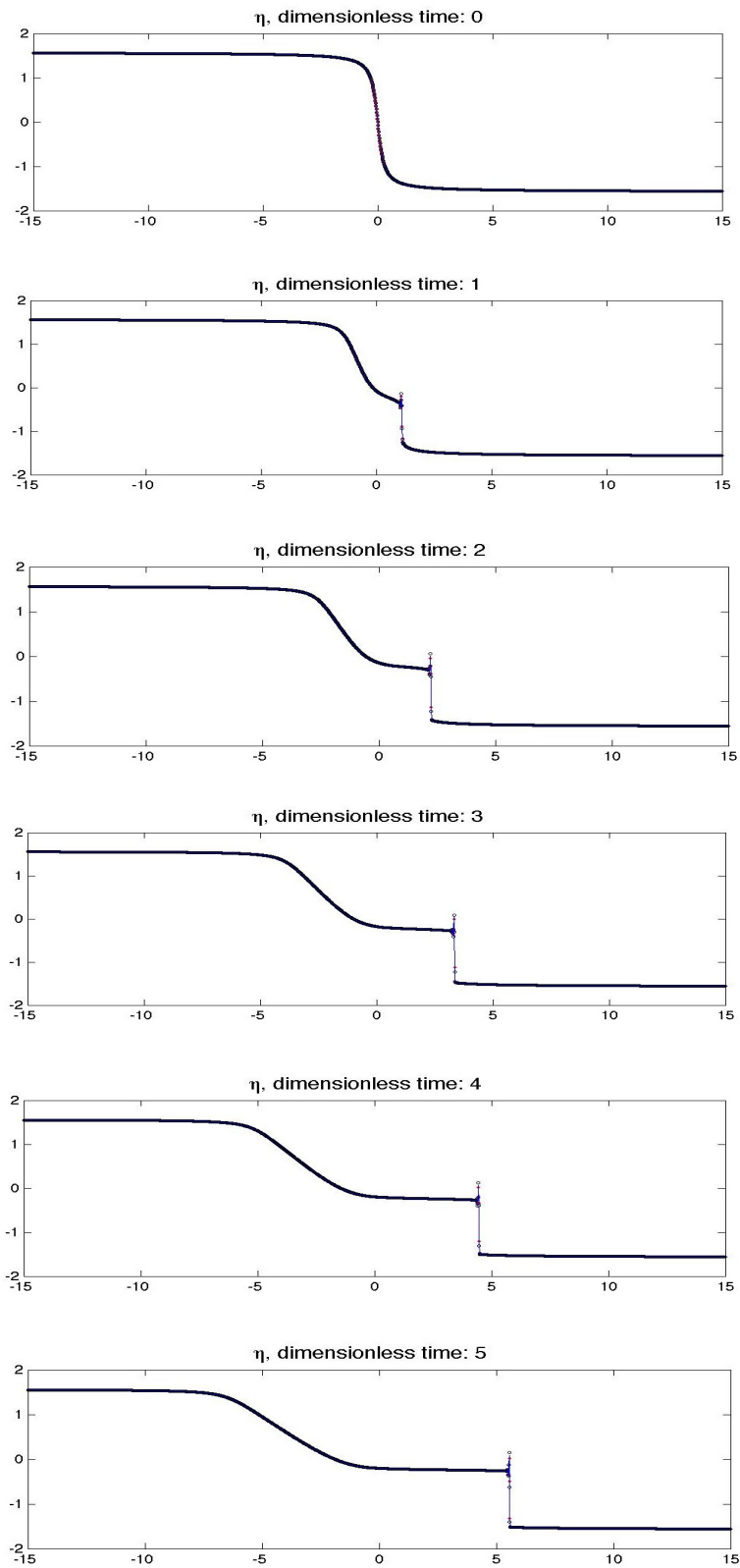
Figure 4.4: The elevation of the fluid,as computed on a fixed mesh, using the initial condition $\eta(x) = -\arctan(5x)$ and 2000 elements.
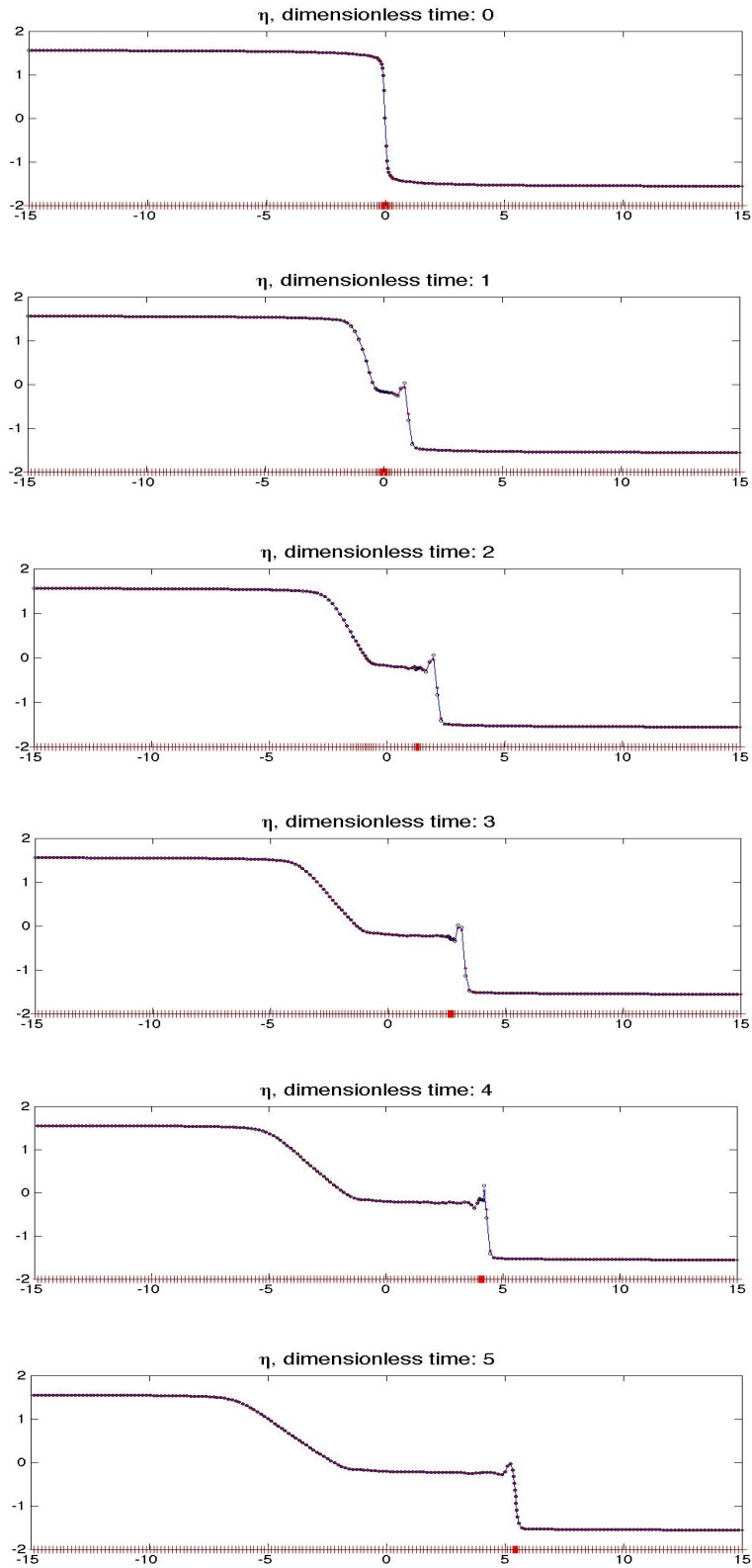
Figure 4.5: The elevation of the fluid, as computed by equidistribution of the arc length of η using the initial condition $\eta(x) = -\arctan(5x)$ and 200 elements. The red marks along the x-axis represent the location of the nodes.
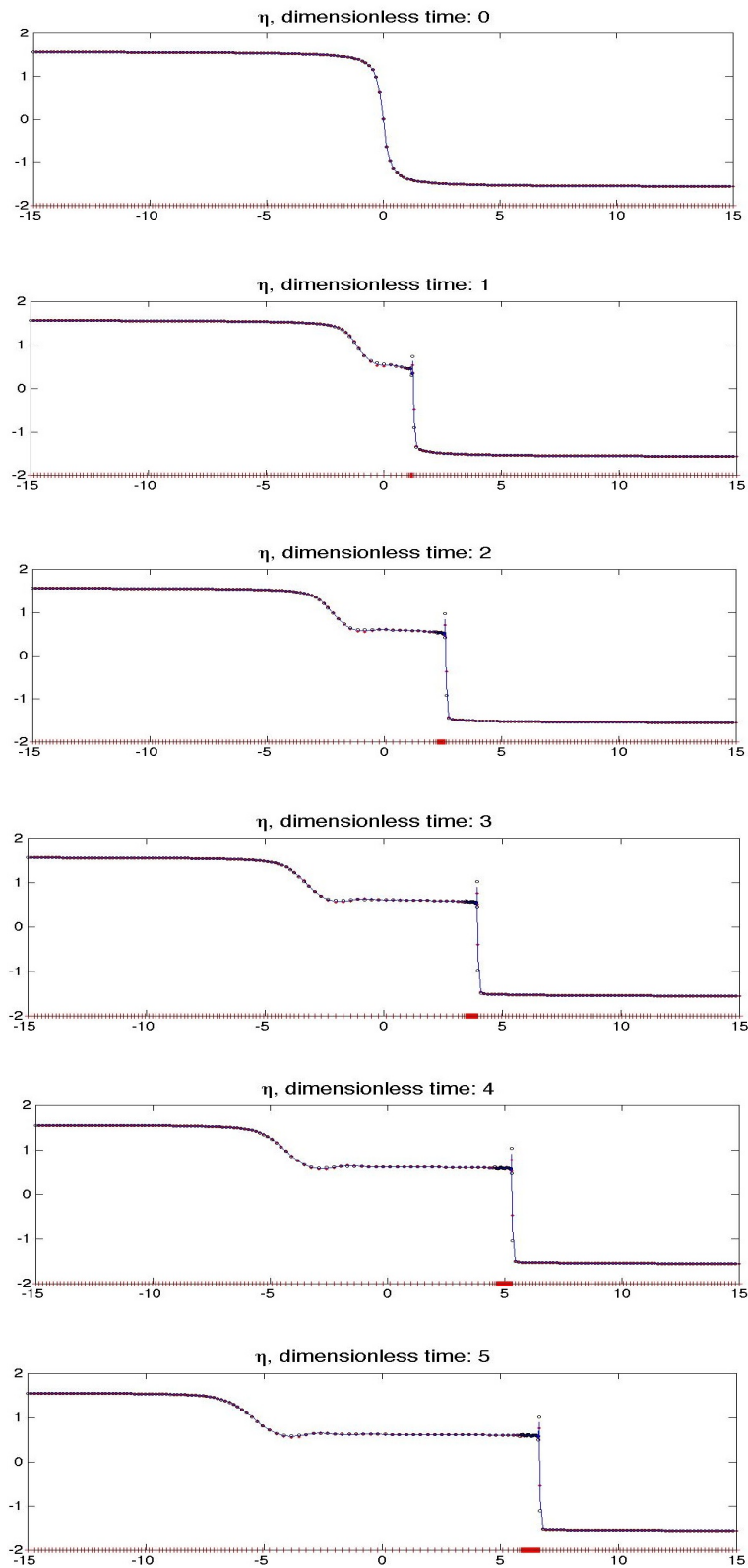
Figure 4.6: Results computed by conserving the volume of each element using the initial condition $\eta(x) = -\arctan(5x)$ and 200 elements. The red marks along the x-axis represent the location of the nodes.

Chapter 5

Numerical Results from the Daly River Model

5.1   The Daly River Model

A more realistic model was developed by E.Hanert [25], which allows variation in the bathymetry and width of the river and has boundary conditions based on real situations. It was designed to model the tidal forcing in the Daly River estuary in Australia which experiences a bore at spring tides. It

Figure 5.1: The Daly River in Australia. (Map sourced from [27].)

has a shallow, funnel shaped estuary, characteristic of rivers which produce a bore. The estuary is about 100km long and its tidal range peaks around 6m during the spring tide. The river discharge varies considerably during the year, from an average of $20\text{m}^3\text{s}^{-1}$ during the dry season (May-September) to over $1000\text{m}^3\text{s}^{-1}$ in the wet season (January-April) [25]. Experiments have
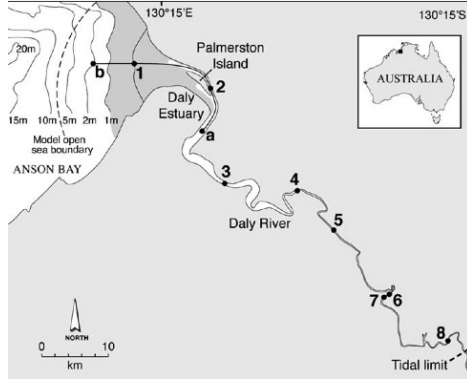
Figure 5.2: The Daly River in Australia and key sites at which experiments were carried out by Wolanski et al. [25]. 2=Palmerston Island, 5=Moon-Billabong, 6,7=Rockbar and 8=Woolianna. (Map sourced from [25])

already been carried out on the bore which occurs on the Daly River [24], [25] and figure 5.2 shows some of the sites.

The shallow water equations are essentially the same as (1.24) and (1.25) with additional terms to represent friction forces and then non-dimensionalized. The equations to be modelled are

$$\frac{\partial u}{\partial t} + \alpha u \frac{\partial u}{\partial x} + \frac{\partial \eta}{\partial x} = -Dr + F, \tag{5.1}$$

$$\frac{\partial \eta}{\partial t} + \frac{\partial}{\partial x}(hu) + \alpha \frac{\partial}{\partial x}(\eta u) = -SB, \tag{5.2}$$

where $\alpha \in [0, 1]$ is a parameter to adjust the importance of non-linear terms, Dr is a bottom drag term, F is the Manning friction and SB allows for variations in the river width. The boundary condition at the mouth of the river is given by setting η to the tidal elevation

$$\eta = \eta_0 \sin(\Omega t)$$

where $\eta_0 = 5$ is the tidal variation and $\Omega = \frac{2\pi}{12}$ sets the length of the tidal cycle. At the top of the estuary the boundary condition is given by setting the velocity proportional to the river discharge. To set the model off we take the initial condition to be a still layer of water, $u(x, 0) = \eta(x, 0) = 0$. This model was again adjusted to accommodate a moving mesh using the two methods of equidistribution of η and conservation of element volume.

5.2   Method of Equidistribution

Again we implement this method as in section 3.2.1, adapting the mesh every second and then interpolating the variables onto the new mesh, again using piecewise cubic Hermite interpolation. Note that we also need to interpolate the river bathymetry and width as well as η and u. After experimentation we found that with $\gamma = 1$ we had very small elements, and even nodes overlapping. Therefore we reduced the gradient effect on the monitor function by setting $\gamma = 0.1$.
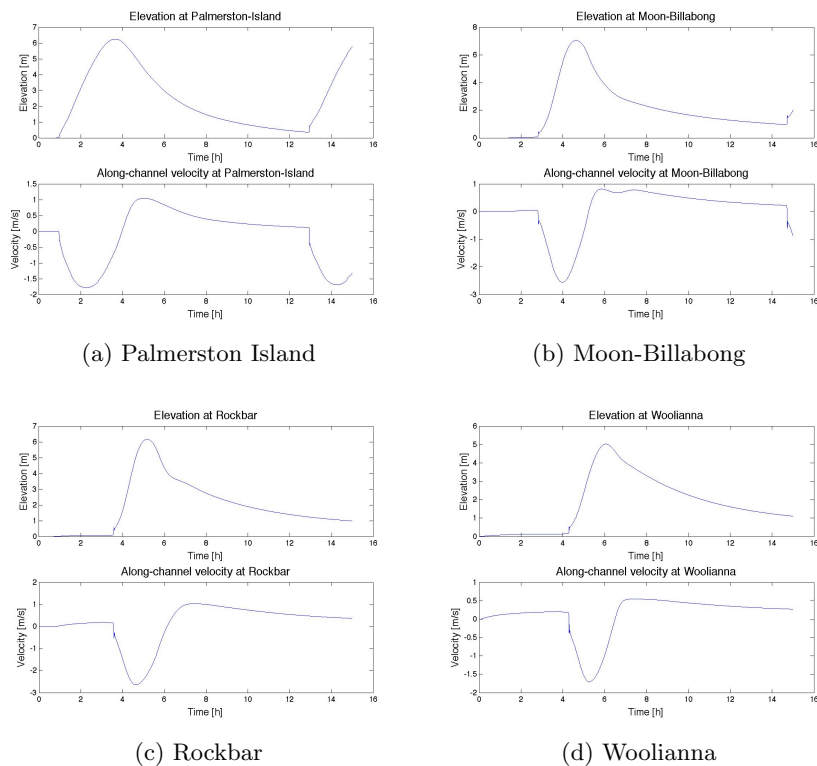
Figure 5.3: Elevation and velocities at the four sites computed on a fixed mesh using 1034 elements and a time step of 0.0001.

Comparing the results, figure 5.7, with those computed on a fixed mesh, figure 5.6, we can see that, although the position of the nodes are increased in density around sharper gradients in the waters elevation, there is not a great difference between the solutions. Comparing the elevation and velocity at the four sites—Palmerston Island, Moon-Billabong, Rockbar and Woolianna— still does not give any indication as to any difference between the models, see figures 5.3 and 5.4.

It would interesting to see how the arc length method performed taking a coarser mesh for this problem. When applied to the basic model there only seemed to be a difference from the fixed mesh solution when large discontinuities were considered, and this became more pronounced when less elements were used. By having a coarser mesh it would also allow us to take γ to be a larger value and therefore the node density will be greater around discontinuities compared to a fixed mesh with an equal number of elements.

5.3 Volume Conservation

In this method we are trying to conserve the volume of each element, but this should only be affected by the change in elevation of the river and not the variation in the bed of the river. As we no longer have a flat lower boundary to our domain it is important that we do not let the varying

33

(a) Palmerston Island
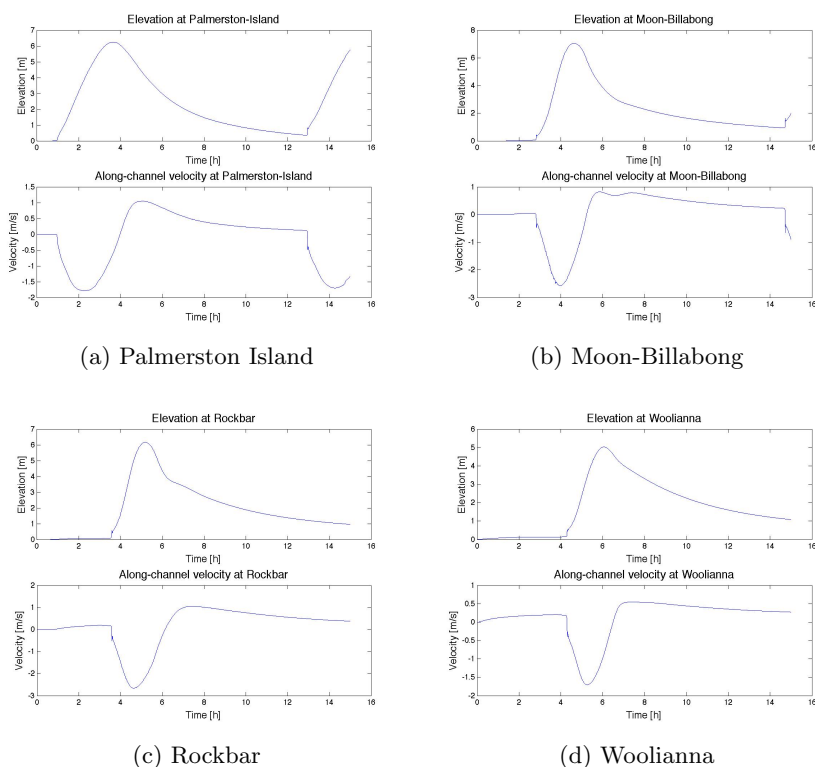
(b) Moon-Billabong

(c) Rockbar

(d) Woolianna

Figure 5.4: Elevation and velocities at the four sites computed from the equidistribution of arc length using 1034 elements and a time step of 0.0001.

bathymetry of the river affect the calculation (3.12) for the mesh velocity. The most obvious choice is to take the height of each element as η, however this can lead to division by numbers close to zero. Therefore we include the minimum river depth h_0 in our element height, which in our dimensionless units is simply 1. Therefore to calculate the mesh velocity we use

$$\dot{b} = u(b) - \frac{\eta(a) + 1}{\eta(b) + 1} \left(u(a) - \dot{a}\right).$$

We again have to alter our equations to allow for the fact that the mesh is now moving, and so we now need to solve

$$\frac{d}{dt} \int \hat{u} \, dx - \int \frac{\partial}{\partial x} \left(\hat{u} \frac{\partial \hat{x}}{\partial t}\right) \, dx + \int \left(\alpha u \frac{\partial u}{\partial x} + \frac{\partial \eta}{\partial x}\right) \, dx = -Dr + F,$$

$$\frac{d}{dt} \int \hat{\eta} \, dx - \int \frac{\partial}{\partial x} \left(\hat{\eta} \frac{\partial \hat{x}}{\partial t}\right) \, dx + \int \left(\frac{\partial}{\partial x}(hu) + \alpha \frac{\partial}{\partial x}(\eta u)\right) \, dx = -SB.$$

After running the model we encountered another problem, the mesh nodes were overtaking each other. In order to prevent this we could take a smaller step size. However, instead I decided to remove nodes when the size of the element became too small, as defined by the CFL condition. They were then repositioned in the centre of the largest element in the domain so the total number of nodes remained constant. The value of the variables

at this new node was given by the average of the values at the nodes either side. This also helped to reduce the possibility that any area of the domain was inadequately covered by nodes.

The results of this method can be found in figure 5.8. It can be immediately seen that the bore is clearly defined using this method and that the bores generated move faster than those generated from a fixed grid. The elevation upstream also never returns to an average level after the bore has passed and the velocity of the river is much greater using this method.
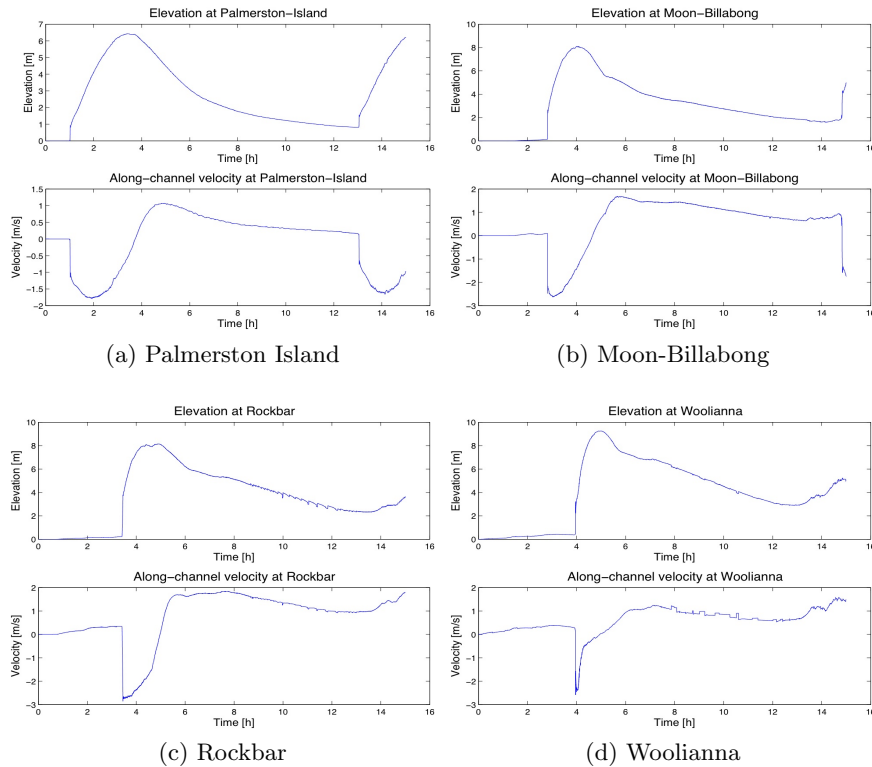

Figure 5.5: Elevation and velocities at the four sites computed from the conservation of the element volume using 1034 elements and a time step of 0.0001.

Looking at the site readings, figure 5.5, we see that near the river mouth, at Palmerston Island, the elevation and velocity readings given by all the models are very similar. At Moon-Billabong and further upstream there is a marked increase in tidal elevation from the volume conserving method. This disagrees with findings by Wolanski et al. [25] which states '..., the tides become increasingly asymmetric and decreased in amplitude with increasing distance from site 1' (as shown in figure 5.2). Also the results from the site at Woolianna become increasingly erratic as time goes on. This suggests that there may be an error in the code for this model at the right hand boundary.

Another cause for concern is the extent to which the nodes tend to congregate in areas where it does not seem required. Although the aim of moving the mesh is to increase the mesh resolution in certain areas, we also do not want to leave other areas too poorly modelled. This seems to be a

problem particularly at the right hand end of the domain, which may be the source of the erratic readings at Woolianna. The reason this area of the domain is so badly affected may be due to the general flow of the river being to the left, the grid points are 'carried along by the current'. One area of further investigation could be to try modifying the mesh velocity to take this into account, perhaps by subtracting the average river discharge.
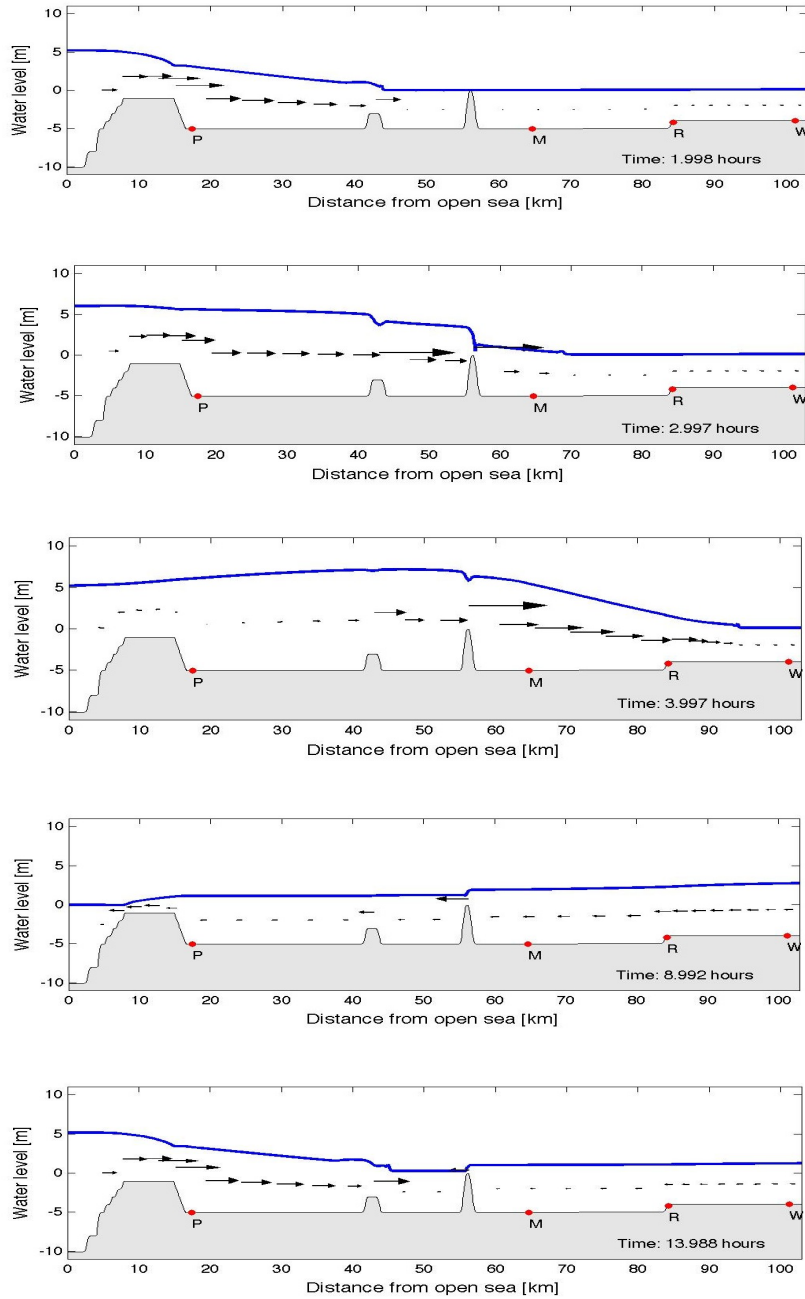
Figure 5.6: Output from the Daly River model using a fixed mesh with 1034 elements and a time step of 0.0001. The lower shaded area represents the river bed, with the water surface indicated by a continuous blue line. Velocities are shown by the arrows, whose size is proportional to the velocity magnitude. The four locations at which readings are taken are indicated; Palmerston Island, Moon-Billabong, Rockbar and Woolianna.
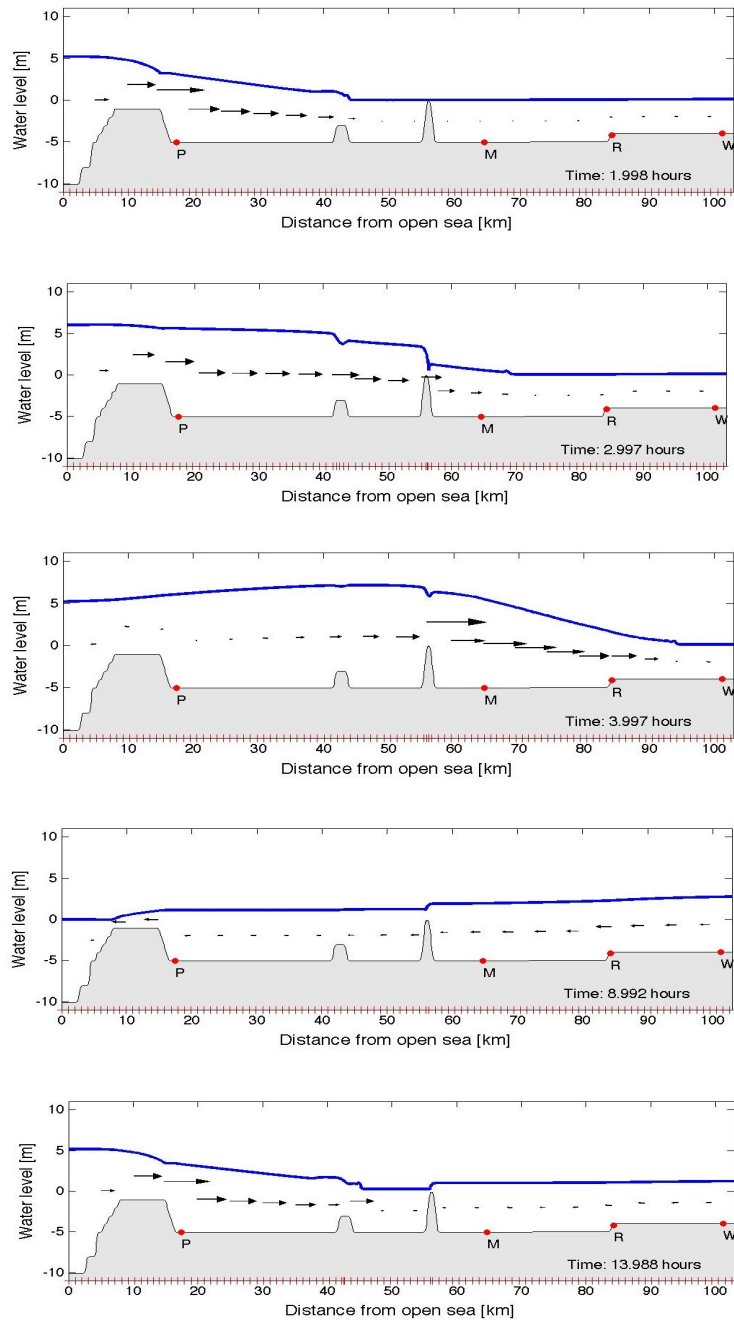
Figure 5.7: Output from the Daly River model using an arc length equidistribution method with 1034 elements and a time step of 0.0001. The lower shaded area represents the river bed, with the water surface indicated by a continuous blue line. Velocities are shown by the arrows, whose size is proportional to the velocity magnitude. The four locations at which readings are taken are indicated; Palmerston Island, Moon-Billabong, Rockbar and Woolianna. The red marks along the x-axis represent every 10 elements.

Figure 5.8: Output from the Daly River model conserving the volume of each element with 1034 elements and a time step of 0.0001. The lower shaded area represents the river bed, with the water surface indicated by a continuous blue line. Velocities are shown by the arrows, whose size is proportional to the velocity magnitude. The four locations at which readings are taken are indicated; Palmerston Island, Moon-Billabong, Rockbar and Woolianna. The red marks along the x-axis represent every 10 elements.
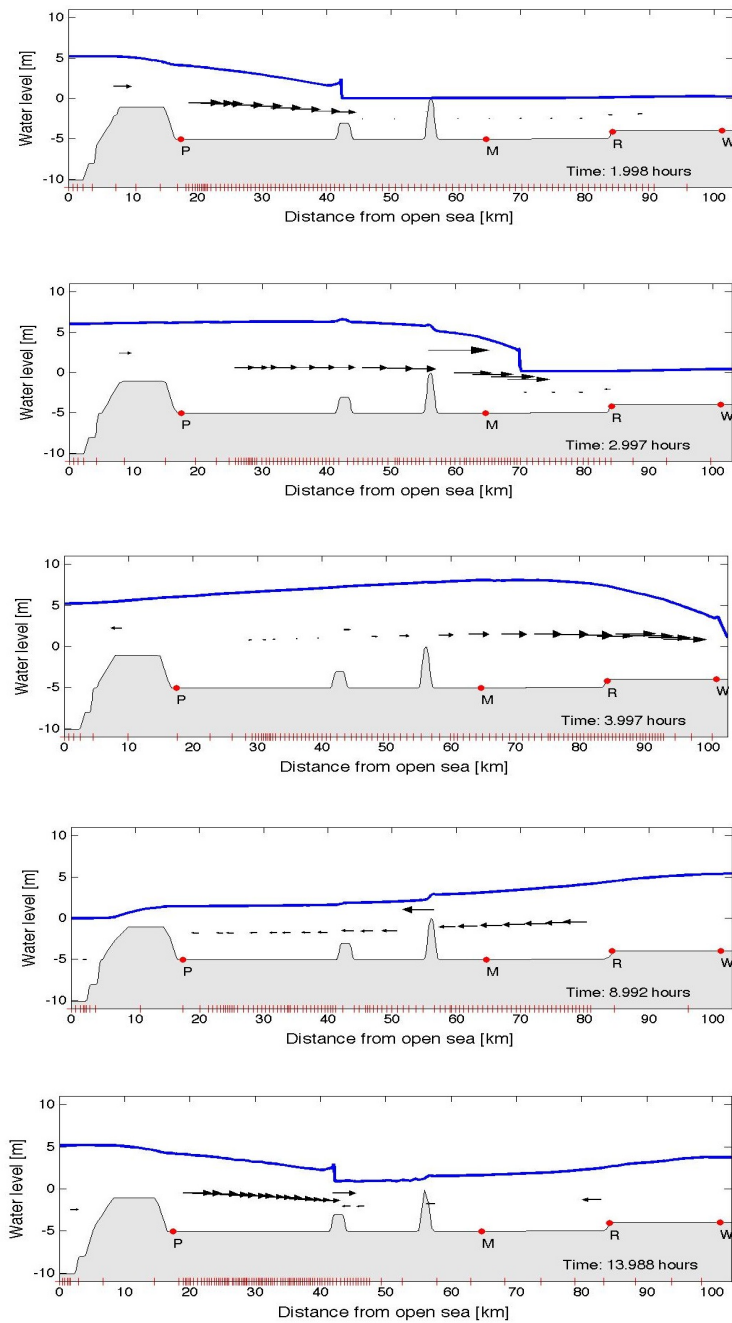
Chapter 6

Summary and Further Work

We have briefly looked at different finite element methods and their ability to capture discontinuous solutions, and then continued on to study a range of approaches to adapting the numerical mesh, focusing on moving mesh methods.

Two of these methods were investigated in detail, namely the method of equidistribution and the conservation of volume method. First they were applied to a simple model in a frictionless rectangular domain. The method of equidistribution did not produce a better result than a fixed mesh, although this may be due to the simplicity of the solution being studied. The volume conservation method did not perform very well at producing an accurate solution, although discontinuities were defined clearly, most likely due to the high density of nodes which became positioned around the shock.

One area of further research would be to apply these methods to problems which have a more complex solution and see how they compare against a fixed grid. The arc length method could also be applied in a more continuous manner by taking the time derivative of the equidistribution principle to calculate nodal velocities. We could also combine these two methods, in effect we would then be conserving the arc length.

We then went on to look at how these methods behaved when applied to a more realistic model. The conservation of volume method again produced distinct discontinuities, however the solution was still highly inaccurate overall, giving solutions which which did not conform to observations. There were also significant problems with mesh tangling. The areas of high node density did not even seem to correspond to areas where the solution was complex with this model.

The equidistribution approach proved better, although without any further increase in accuracy than a fixed grid. However I think that when the number of elements is reduced the equidistribution will prove more accurate than a fixed grid, and this is another area which needs further study. Also further approaches to calculate the nodal velocities could be investigated.

Bibliography

[1] Baines, M.J. (1998). Grid adaptation via node movement. *Applied Numerical Mathematics* 26, 77-96.

[2] Baines, M.J., Hubbard, M.E., Jimack, P.K., (2005). A moving mesh finite element algorithm for the adaptive solution of time-dependent partial differential equations with moving boundaries. *Applied Numerical Mathematics* 54, 450-469

[3] Cao, W., Huang, W., Russell, R.D., (2003). Approaches for generating moving adaptive meshes: location versus velocity. *Applied Numerical Mathematics* 47, 121-138

[4] Chandrupatla, T.R., Belegundu, A.D. (2002). Introduction to Finite Elements in Engineering, 3rd edition. *Prentice Hall*

[5] Clough, R.W. (1960). The finite element method in plane stress analysis. *Proceedings American Society of Civil Engineers* 2nd Conference on Electronic Computation, Pittsburgh, Pennsylvania, 23:345-378

[6] Courant, R. (1943). Variational methods for the solution of problems of equilibrium and vibrations. *Bulletin of the American Mathematical Society* 49:1-23

[7] Donnelly, C., Chanson, H. (Sept 2002). Environmental impact of tidal bores in tropical rivers. *Proc. 5th Intl River Management Symp.*, Brisbane, Australia

[8] Dwyer, H.A., Kel, R.J., Sanders, B.R. (1980). Adaptive grid methods for problems in fluid mechanics and heat transfer. *AIAA J.* 18

[9] Fennema, R.J., Chaudry, H.M. (1987). Simulation of one-dimensional dam-breakflow. *J. Hydraul. Res.* 25 41-51

[10] Ferziger, J.H., Perić, M. (1999). *Computational Methods for Fluid Dynamics* 2nd *Ed.* Springer

[11] Glaister, P. (1987) Difference Schemes for the Shallow Water Equations *Numerical Analysis Report 9/87, Dept. of Math., University of Reading*

[12] Hanert, E., Le Roux, D.Y., Legat, V., Deleersnijder, E. (2004). Advection schemes for unstructured grid ocean modelling. *Ocean Modelling* 7, 39-58

[13] Hindman, R.G., Kutler, P., Anderson, D.A.(1979). A two-dimensional unsteady Euler-equation solve for flow regions with arbitrary boundaries. *AIAA paper* 76-1465

[14] Katopodes, N.D., Strelkoff, T. (1978). Computing two-dimensional dam-break flood waves. *J. Hydraul. Div. ASCE* 1269-1287

[15] Kuo, A.C., Polvani, L.M. (1997). Time-Dependent Fully Nonlinear Geostrophic Adjustment. *Journal of Physical Oceanography* 27 1614-1634

[16] Miller, K., Miller, R.N. (1981). Moving finite elements I. *SIAM J. Numer. Anal.* 18 1019-1032

[17] Miller, K. (1981). Moving finite elements II. *SIAM J. Numer. Anal.*18 1033-1057

[18] Rahman, M., Chaudhry, M.H. (1998). Simulation of dam-break flow with grid adaptation. *Advances in Water Resources* 21 1 1-9

[19] Rai, M.M., Anderson, D.A. (1982). Application of adaptive grids to fluid-flow problems with asymptotic solutions. *AIAA J.* 20 496-502

[20] Stoker, J.J., 1958. *Water Waves.* John Wiley.

[21] Strang, G., Fix, G.J. (1973). An Analysis of the Finite Element Method. *Prentice Hall*

[22] White, L., Legat, V., Deleersnijder, E., Le Roux, D. (2006). A one-dimensional benchmark for the propagation of Poincaré waves. *Ocean Modelling* 15 101-123

[23] Witham, G.B. (1974). *Linear and Non-linear Waves* John Wiley

[24] Wolanski, E., Williams, D., Spagnol, S., Chanson, H. (2004). Undular tidal bore dynamics in the Daly Estuary, Northern Australia. *Estuarine, Coastal and Shelf Science* 60 629-636

[25] Wolanski, E., Williams, D., Hanert, E. (2006). The sediment trapping efficiency of the macro-tidal Daly Estuary, tropical Australia *Estuarine, Coastal and Shelf Science* 69, 291-298

[26] http://www.tidalbore.info/

[27] http://www.petitcodiac.org/riverkeeper/english/tidalbore/WorldBores/world.htm